

Neutron emission spectroscopy of fusion plasmas with a NE213 liquid scintillator at JET

Federico Binda

Licentiate Thesis

*Department of Physics and Astronomy
Uppsala University*

2015

Abstract

Neutron diagnostics will play a fundamental role in future fusion plasma machines, where the harsh environment will make the use of many other type of diagnostics practically impossible. Complex techniques to measure the neutron spectrum emitted from tokamak plasmas have been developed over the years, producing state of the art neutron spectrometers. However, recently compact neutron spectrometers have been gaining the interest of the research community. They are much simpler to operate and maintain, have lower cost and they can be employed in the channels of a neutron camera, providing profile measurements. The drawbacks are that they have a worse resolution and a response to neutrons that is not optimal for spectroscopy.

The goal of the work presented in this thesis is to estimate to which extent a compact detector such as a NE213 liquid scintillator can be used to perform neutron emission spectroscopy analysis.

The detector used for this study was installed in the back of the MPRu spectrometer at JET in 2012. The characterization of the response of the detector was done using a combination of MCNPX simulations and real measurements. The data analysis was performed using the forward fitting approach: a model of the neutron spectrum is produced, then folded with the response of the detector and finally compared with the data. Two types of plasma scenarios were analyzed, one with NBI heating only, and another with NBI and third harmonic radio-frequency heating. In both cases the TOFOR spectrometer was used as a reference to estimate the parameters in the model of the neutron spectrum.

The results are promising and suggest that neutron spectroscopy can be performed with NE213 scintillators although the quality of the results, as given by performance indicators such as uncertainties, is much lower than the performance of high resolution spectrometers.

List of papers

This thesis is based on the following papers

Paper I

Monte carlo simulation of the data acquisition chain of scintillation detectors

F. Binda, G. Ericsson, C. Hellesen, A. Hjalmarsson, J. Eriksson, M. Skiba, S. Conroy and M. Weiszflog

Proceedings of the *International Conference on Fusion Reactor Diagnostics*, September, 9–13, 2013, Varenna (LC), Italy. *AIP Conf. Proc.* **1612** (2014) 101.

My contribution: Developed and tested the code; wrote the paper.

Paper II

Forward fitting of experimental data from a NE213 neutron detector installed with the magnetic proton recoil upgraded spectrometer at JET

F. Binda, G. Ericsson, J. Eriksson, C. Hellesen, S. Conroy, E. Andersson Sundén and JET EFDA Contributors

Proceedings of the *20th Topical Conference on High-Temperature Plasma Diagnostics*, June, 1–5, 2014, Atlanta, Georgia, USA. *Rev. Sci. Instrum.* **85** (2014) 11E123.

My contribution: Performed the calibration, the MCNPX simulations, the data analysis and the error estimate; wrote the paper.

Paper III

Analysis of the fast ion tails observed in the NE213 pulse height spectra measured during third harmonic radio-frequency heating experiments at JET

F. Binda, J. Eriksson, G. Ericsson, C. Hellesen, S. Conroy, M. Cecconello, M. Nocente, C. Cazzaniga, E. Andersson Sundén and JET Contributors

Manuscript.

My contribution: Performed the corrections for pile-up, count rate and triton burn-up; performed the response calculation and the data analysis; wrote the paper.

Contents

Preface	9
1 Introduction to nuclear fusion	11
2 Magnetically confined fusion	13
2.1 Tokamak	14
2.1.1 JET	14
2.2 Heating methods	15
3 Fusion neutrons	17
3.1 Neutron emission spectroscopy	18
4 Neutron diagnostics	19
4.1 Quality of a neutron spectrometer	19
4.2 The magnetic proton recoil technique	19
4.3 TOFOR	20
4.4 Compact spectrometers	22
4.4.1 Liquid scintillators	22
4.5 Comparison between spectrometers	24
5 The “Afterburner” installation	27
5.1 Detector specifications and assembly	27
5.2 Line of sight and Field of view	28
6 Afterburner system characterization	31
6.1 Typical pulses	31
6.2 Pulse shape discrimination	31
6.3 MCNPX model	34
6.4 Gamma and neutron calibration	36
7 Dacsim - Data acquisition chain simulation (Paper I)	41
7.1 The code	41
7.2 Examples	42
8 Data analysis	45
8.1 Data processing	45
8.1.1 Gain drift	45

8.1.2	Pile-up rejection	47
8.2	Analysis of the neutron pulse height spectra	47
8.2.1	Thermal fraction estimate (Paper II)	49
8.2.2	Third harmonic radio-frequency heating analysis (Paper III)	53
9	Conclusions	57
	Acknowledgments	59

Preface

When I started working on this project, back in 2011, I was still a master student. At the time the idea behind the so-called “Afterburner” installation was to enhance the time resolution of the neutron flux measurement of the MPRu during DD operations. After the detector was installed in 2012 and we started collecting data, we realised that there were many other interesting paths that we could explore. We started investigating the possibility of performing neutron emission spectroscopy analysis of the spectra that we had collected. The task was certainly not an easy one, especially considering that the Afterburner detector was never meant to be used as a spectrometer and therefore its response to neutrons had not been measured. However it was also a very exciting challenge, because such detailed spectroscopy work with a NE213 scintillator had not been attempted before. We went down that road and this thesis is the result of all the effort we have put into this during the last three years.

Federico Binda
April 21, 2015

1 Introduction to nuclear fusion

The growing world energy demand calls for technologies that can provide clean, cheap and virtually unlimited energy. Nuclear fusion has the potential to fulfill such requirements, and is therefore subject to thorough investigation by scientists, in the attempt to find an efficient and practical way to obtain a net energy output from it [1].

The basic principle of fusion is, as the word says, the merging of two nuclei. The products of this process are a heavier nucleus and a light particle. If the total mass of the products is lower than the total mass of the reactants, the reaction gives a positive energy output, according to the famous relationship:

$$E = \Delta m \cdot c^2. \quad (1)$$

Table 1 presents the most relevant fusion reactions for energy production. The DT reaction is considered the best candidate for future reactors, because it has a higher energy release and a higher cross section than the other candidates (Figure 1). However research reactors work mostly with the DD reaction, to avoid practical issues related to the handling of tritium, which is radioactive.

Table 1: Fusion reactions relevant for energy production.

Reaction	E_N (MeV)	E_{TOT} (MeV)	Branching Ratio
$d + d \rightarrow {}^3He + n$	2.5	3.3	0.5
$d + d \rightarrow p + t$	-	4.03	0.5
$d + {}^3He \rightarrow {}^4He + p$	-	18.4	1
$d + t \rightarrow {}^4He + n$	14.0	17.6	1

Fusion can only occur if the nuclei get close enough that the strong nuclear forces overcome the Coulomb repulsion. In the sun, for example, this is accomplished thanks to the very high pressure generated by the gravitational field.

One possibility to obtain controlled fusion in a laboratory environment is to heat the fuel to very high temperatures. This transforms the fuel into a plasma, a state of matter which can be described, in a very simplistic way, as a gas made of ionized particles.

The temperatures reached are so high that the fuel would melt any containing material. One way to deal with this problem is to use magnetic fields to confine the fuel in a defined region of space and keep it away from the walls of the containing vessel. The plasma particles are charged, therefore they are forced to follow the

magnetic field lines. Magnetically confined fusion is the center of this work and will be discussed more in detail in the next chapter.

Another way to obtain controlled fusion which is important to mention is inertial confinement. In inertial confinement fusion the fuel is made into a small pellet that is heated and compressed using very strong laser beams [2].

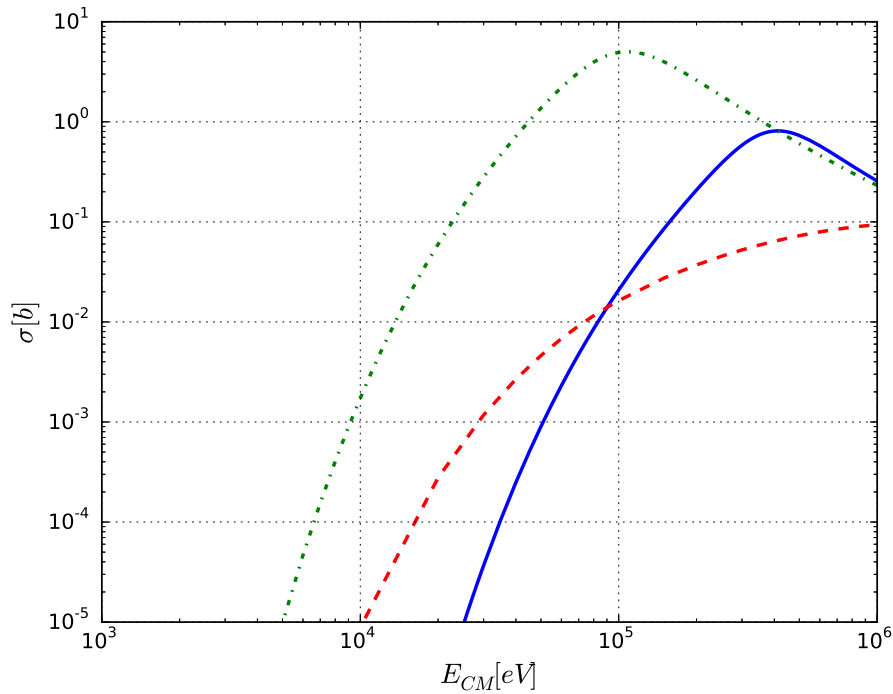


Figure 1: Cross section versus center of mass energy for the ${}^3\text{He}(d, p)\alpha$ (blue solid), $d(d, n){}^3\text{He}$ (red dashed) and $d(t, n)\alpha$ (green dash-dotted) reactions.

2 Magnetically confined fusion

Magnetic fields can be used to control the trajectories of the ionized particles that form a fusion plasma [3]. The Lorentz force makes the charged particles follow the field lines in a helical orbit as shown in Figure 2. Therefore a smart choice of the field lines can trap the plasma particles in a defined region of space.

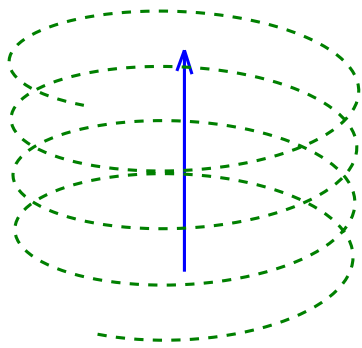


Figure 2: Trajectory of a charged particle (dashed green) in a magnetic field (solid blue arrow).

The first attempts to obtain magnetic confinement were done using magnetic mirrors. In a magnetic mirror the field lines are arranged in a cylindrical shape, parallel to the axis of the cylinder, with the intensity of the field increasing at the ends. A charged particle moving towards one of the ends of the cylinder sees an increasing intensity of the magnetic field. It can be shown that the magnetic field gradient generates a force acting on the particle, with direction towards the lower field region in the center of the cylinder. This means that the parallel velocity of the particle will decrease and eventually change sign, trapping the particle within a well defined region of space. However this mechanism is not perfect, since particles that have a parallel velocity high enough will not be reflected and will escape at the end of the cylinder.

To improve this idea it was proposed to bend the lines to form a toroidal shape, so that there are no ends where the particles can escape. This is the basis point

for the development of the tokamak, the configuration which is currently viewed as the most promising for magnetic fusion [4].

2.1 Tokamak

The word Tokamak comes from the Russian acronym “toroidal’naya kamera s magnitnymi katushkami”, which translated to English is “toroidal chamber with magnetic coils”. The configuration of the magnetic field in a tokamak is depicted in Figure 3. The toroidal coils produce the toroidal component of the magnetic field; The poloidal component of the field is produced by inducing a toroidal current in the plasma. The resulting magnetic field is composed of twisted toroidal lines (Figure 3). The twisting is necessary to avoid the creation of electric fields that could destroy the confinement of the plasma.

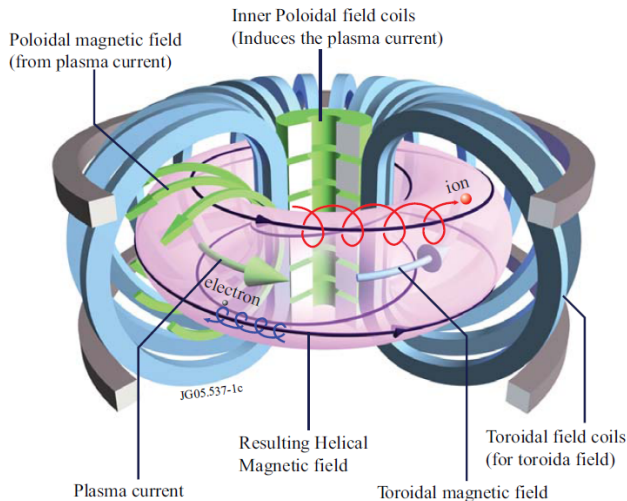


Figure 3: Configuration of the magnetic field in a tokamak. Figure from www.euro-fusion.org

2.1.1 JET

The work presented in this thesis was carried out at the the Joint European Torus (JET). JET is currently the largest tokamak in the world [5], with a major radius of about 3 m and the total plasma volume is about 100 m^3 . It was built in the end of the 70s in Culham, a small village outside Oxford in England; it started operations in 1983 and in 1997 obtained the world record of fusion power produced, 16 MW. Figure 4 shows the JET torus hall and the interior of the JET vacuum vessel.

The next step towards a fusion tokamak reactor is ITER, which is currently being built in Cadarache, France, and is expected to start operations in 2020. The ITER tokamak will have a major radius of 6 m and a plasma volume of 840 m³ and the goal is to produce 500 MW of fusion power.

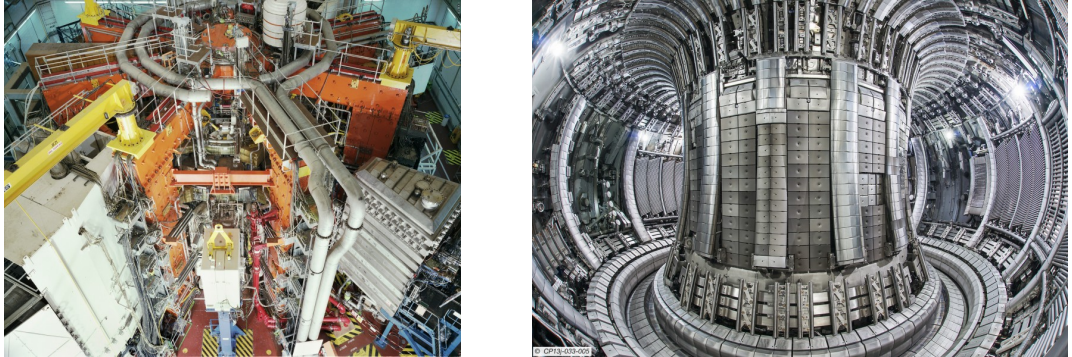


Figure 4: Picture of the JET torus hall (left) and the interior of the JET vacuum vessel (right). Figures from www.euro-fusion.org

2.2 Heating methods

Before going into the discussion of the heating methods, it is convenient to introduce the definition of temperature that is commonly used in plasma physics:

$$T = kT_{\text{Kelvin}}, \quad (2)$$

where k is the Boltzmann constant and T_{Kelvin} is the temperature in Kelvin. With this definition the plasma temperature is given in eV. As an example, a temperature of 1 eV corresponds to about 11600 K.

There are three main methods for external heating of the plasma and one internal heating mechanism. The internal heating is due to the α particles generated in the DT reaction. If the α particles are well confined they can heat up the plasma by exchanging their energy with the deuterons or the tritons.

The external heating methods are: ohmic heating, neutral beam injection (NBI) and radio frequency (RF) heating. There are different types of RF heating, but in this thesis we will deal only with ion cyclotron resonance frequency heating (ICRH).

Ohmic heating consists in driving a current inside the fuel, which will dissipate heat because of the resistance of the plasma. However the resistance of the plasma is proportional to $T^{-3/2}$, therefore this technique will be less effective when high temperatures are reached. At JET ohmic heating can raise the temperature up to

about 2 keV. NBI or ICRH, which are commonly referred to as auxiliary heating, are necessary to reach higher temperatures.

The principle behind neutral beam injection is the introduction of highly energetic neutral particles in the plasma. The particles must be neutral to avoid any bending of their trajectory by the strong magnetic field of the tokamak. Once inside the plasma they get quickly ionized and get thermalized, transferring their energy to the plasma particles and becoming plasma particles themselves.

Finally ICRH is based on the transfer of energy from radio-frequency waves to ions, thanks to the resonance between the frequency of the injected electromagnetic wave and the ion cyclotron rotation frequency. ICRH also induces highly energetic ions (up to a few MeV) in the plasma.

3 Fusion neutrons

Two of the fusion reactions shown in Table 1 produce neutrons. The DD reaction emits neutrons at about 2.5 MeV while the DT reaction neutrons have an energy of about 14 MeV. One must be aware that even with a pure deuterium fuel there will be tritons generated by the second reaction in Table 1. These tritons can interact with the deuterons and produce 14 MeV neutrons which are commonly referred to as triton burn-up neutrons (TBN). TBN usually account for about 1% of the total neutron emission from a DD plasma.

Neutrons are not charged, therefore they are not trapped by the magnetic field, and they leave the plasma unaffected. Some of the properties of the escaping neutrons, e.g. their energy, are dependent on the plasma conditions. The measurement of such properties is therefore an indirect measurement of the related plasma properties [6].

There are two main quantities that are of particular interest in fusion applications of neutrons: the neutron flux and the neutron energy distribution.

The former is directly related to the power produced in the reactor. Each neutron produced corresponds to a fusion reaction in the plasma and each reaction releases a known amount of energy. Counting the number of neutrons produced per seconds gives an estimate of the number of reactions per second, which in turn can be used to estimate the energy production per second. When both DD and DT reactions are involved, the power produced is:

$$P = Y_{n,DT} \cdot Q_{DT} + Y_{n,DD} \cdot \left(Q_{n,DD} + Q_{p,DD} \frac{BR_p}{BR_n} \right), \quad (3)$$

where Y denotes the neutron yield, i.e. the total number of neutron produced by the reaction, Q denotes the total energy release of each reaction, BR denotes the branching ratio of a reaction, and the subscripts n and p stand for the neutron and proton producing branch of the DD reaction. The fact that the DD reaction has two branching ratios, of which only one produces neutrons, needs to be taken into account in the multiplicative factor for $Y_{n,DD}$, as done in the equation above.

The neutron energy distribution instead is connected to the velocity distribution of the ions in the plasma. In fact the neutron energy is given by the formula [7]:

$$E_n = \frac{1}{2} m_n v_{cm}^2 + \frac{m_r}{m_n + m_r} (Q + K) + v_{cm} \cos \theta \left(\frac{2m_n m_r}{m_n + m_r} (Q + K) \right)^{1/2}, \quad (4)$$

where the subscripts cm , n , r denote center of mass, neutron and residual nucleus, K is the relative kinetic energy of the reactants and θ is the angle between the velocity of the emitted neutron and the relative velocity of the reactants in

the center of mass frame (Figure 5). The velocity of the ions is represented in the equation through the terms K and v_{cm} . Therefore measuring the energy distribution of the neutrons means diagnosing indirectly the velocity distribution of the ions in the plasma.

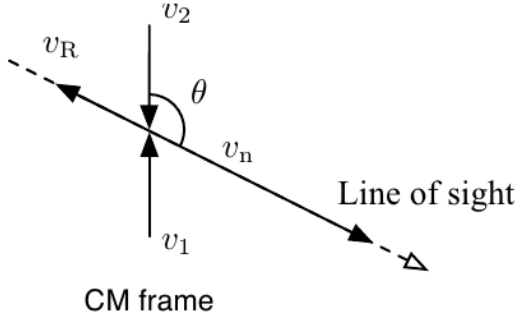


Figure 5: The kinematics of a fusion reaction in the center of mass frame.

3.1 Neutron emission spectroscopy

Neutron emission spectroscopy (NES) is the analysis of the energy distribution of the neutrons emitted by the plasma. Equation 4 describes the relationship between the energy of an emitted neutron and the velocity of the ions that produced it. From a given ion velocity distribution in the plasma one can, in principle, obtain the expected emitted neutron spectrum. In practice this can be done analytically only in few very simple cases, e.g. for Maxwellian ion distributions, therefore normally numerical calculations are employed [6].

The ions in the plasma may be separated into populations, depending on their origin. For example in a NBI heated plasma there are thermal ions (the ions already thermalized inside the plasma) and beam ions (the ions introduced by the beams which have not been thermalized yet). As mentioned before, the energy of a neutron reflects the energy distribution of the ions that produced it, therefore interactions between ions belonging to different populations produce neutron energy distributions with different shapes. The total neutron spectrum can therefore be divided into components, each generated by a different combination of ion populations. In the case of NBI heated plasma there are three spectral components: thermal-thermal, beam-thermal and beam-beam.

4 Neutron diagnostics

Neutrons are neutral, thus cannot be detected directly. The techniques used to detect neutrons rely on the conversion of the neutron into another particle, normally a proton or a heavier ion, which is charged and can therefore be detected for example with a scintillator. In the case of energy measurements, the quantity directly detected by the spectrometer is not the neutron energy but some other quantity that is related to it. For example in the time of flight technique the time of flight of the neutron, which depends on the neutron energy, is what is actually measured (more on the time of flight technique in section 4.3).

4.1 Quality of a neutron spectrometer

There are three instrumental properties that can be used to evaluate the quality of a neutron spectrometer: the efficiency, the resolution and the shape of the response of the spectrometer to neutrons.

The efficiency is simply the number of neutrons detected per number of incident neutrons. A more efficient spectrometer gives more counting statistics, therefore can allow either a finer time resolution or a more precise result in the same integration time.

The resolution is the gaussian broadening of the spectra measured by the spectrometer. A better resolution means that it is possible to distinguish between finer features in the spectrum.

Finally the response function of the spectrometer is the spectrum produced by monoenergetic neutrons. Ideally the best response would be a delta function, but the various processes involved in the conversion of the neutron energy into a secondary quantity introduce distortions to this ideal response. In general, if the response is closer to the ideal response, the analysis of the spectra is easier and more precise.

4.2 The magnetic proton recoil technique

The magnetic proton recoil (MPR) technique is based on the conversion of neutrons into protons via elastic scattering in a thin plastic foil and the subsequent momentum separation of the recoil protons in a magnetic field.

An instrument based on this technique was installed by the Uppsala Neutron Diagnostic Group at JET in 1996, inside the torus hall, and it was upgraded (MPRu) with digital acquisition boards in 2005 [8]. It was optimized for 14 MeV neutron measurements, but it can be used to measure 2.5 MeV neutrons too.

The main components of the MPRu spectrometer are shown in Figure 6. The neutrons emitted by the plasma are formed into a "neutron beam" by a collimator.

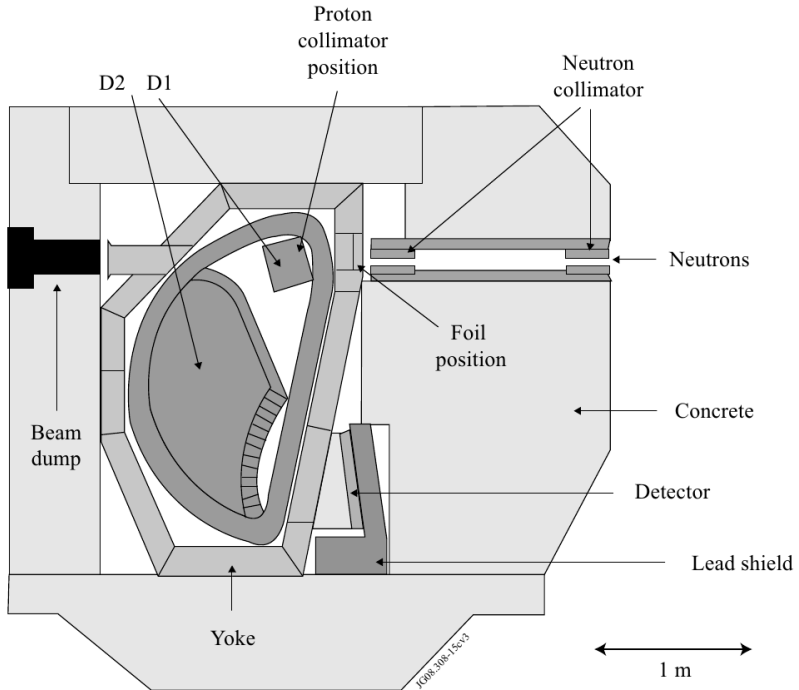


Figure 6: Components of the MPRu spectrometer.

They then enter the spectrometer's vacuum chamber through a thin steel window and impinge on a thin polythene foil, where they interact with protons via elastic scattering. Some of the protons are scattered in the forward direction (same direction of the incoming neutrons) and they pass through the proton collimator. The relationship between neutron and proton energy is $E_p = E_n \cos^2 \theta$, where θ is the scattering angle in the laboratory system. Thus a proton scattered in the forward direction ($\theta = 90^\circ$) has the same energy as the original neutron. Inside the vacuum chamber two magnetic dipoles (D1 and D2) generate a magnetic field that bends the trajectories of the protons towards the hodoscope, an array of plastic scintillation detectors. The bending radius of the protons inside the magnetic field is proportional to their velocity ($r = mv/Bq$), therefore different energies will correspond to different positions of impact on the hodoscope.

4.3 TOFOR

The Time Of Flight spectrometer Optimized for high Rate (TOFOR) was installed in the JET roof lab (above the tokamak) by the Uppsala group in 2005 [9]. It is mainly a 2.5 MeV spectrometer but it can also measure 14 MeV neutrons. The principle of this spectrometer is the measurement of the time that it takes for

a neutron to cover a certain distance. This time is related to the energy of the neutron through the equation $E_n = 2m_n d^2/t_{TOF}^2$, where d is the length of the flight path and m_n is the neutron mass.

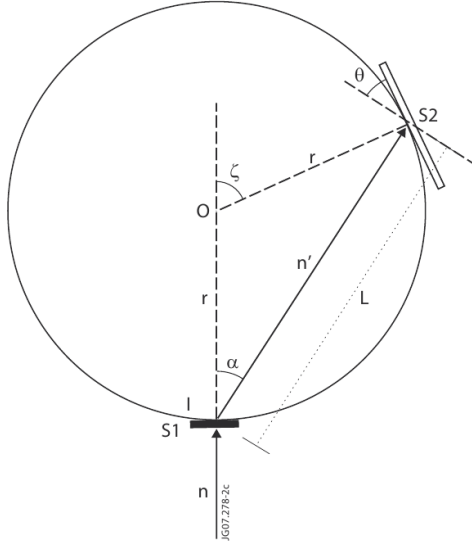


Figure 7: Geometry of the TOFOR spectrometer. From [9]

The geometry of the TOFOR instrument is shown in Figure 7. The neutrons from the plasma are formed into a collimated “neutron beam” through a 2 meter long aperture in the JET roof laboratory floor. Some of the incoming neutrons scatter in a first set of detectors (S1) which gives the start time. Some of the scattered neutron are subsequently detected in a second set of detectors (S2), that gives the stop time. The S2 detectors are placed at an angle $\alpha \neq 0$ with respect to the incoming neutron flux. The time of flight measured is therefore that of a scattered neutron with scattering angle α , which is related to the original neutron energy by the equation:

$$E'_n = E_n \cos^2(\alpha) = \frac{1}{2} m_n \frac{L^2}{t_{tof}^2}. \quad (5)$$

Noticing that $L = 2r \cos(\alpha)$ the original neutron energy is simply obtained from:

$$E_n = \frac{1}{2} m_n \frac{r^2}{t_{tof}^2}. \quad (6)$$

4.4 Compact spectrometers

The spectrometers described so far are complex systems with a lot of components. Simpler and cheaper alternatives are the so-called compact spectrometers, such as semiconductors (silicon and diamonds) and scintillators (organic and inorganic solids and liquids). The problems with the compact spectrometers are that their resolution is usually worse than for the optimized spectrometers and their response to neutrons is not optimal for energy measurements (more in section 4.5).

4.4.1 Liquid scintillators

Liquid scintillators are usually made of organic compounds, therefore they contain mainly hydrogen and carbon atoms [10]. At the energies of interest for DD fusion neutrons interact with hydrogen and carbon nuclei via elastic scattering. Other reaction channels on carbon such as $^{12}C(n, \alpha)^9Be$, $^{12}C(n, p)^{12}B$, and $^{12}C(n, d)^{11}B$ become important only for neutron energies above 7 MeV.

The scattered proton is charged, therefore it is slowed down by interacting with the electrons in the material, which results in the excitation of molecular levels in the scintillator. The consequent de-excitation produces light in the visible range, with a total intensity proportional to the energy deposited by the proton. The light produced from scattering on carbon is much less than that from hydrogen, so it contributes only to the low energy part of the measured spectrum [11]. The light pulse produced can then be converted into a current pulse using a Photomultiplier Tube (PMT). The PMT is composed of a photo-cathode that converts photons into electrons through the photoelectric effect, and then a series of dynodes that multiplies the electrons, which are finally collected by an anode. The integral of the current pulse (total charge) is directly proportional to the intensity of the light collected by the photocathode, therefore it is proportional to the energy deposited in the scintillator. The spectrum constructed from the total charge of the events is referred to as pulse height spectrum (PHS).

There are several factors that contribute to the resolution of a detector based on (liquid) scintillation and PMT:

1. spatial fluctuations in the light collection efficiency from different parts of the scintillation volume;
2. statistical variations in the number of photo-electrons produced and in the multiplication process in the PMT;
3. electrical noise on the signal.

These three effects are represented in the following empirical equation by the terms α , β , and γ respectively:

$$R(E) = \frac{FWHM(E)}{E} = \sqrt{\alpha^2 + \frac{\beta^2}{E} + \frac{\gamma^2}{E^2}}, \quad (7)$$

where R is the relative resolution, E is the deposited energy in MeVee (mega electronvolt electron equivalent), and $FWHM$ stands for full width at half maximum.

Furthermore, if the pulses are recorded using a waveform digitizer, the resolution could be deteriorated if the bit resolution and sampling frequency of the digitizer are not chosen appropriately.

In a similar way to that for neutron detection, liquid scintillators can also detect gamma particles, the difference being that the gammas interact with electrons (mainly via Compton scattering) instead of protons. However some scintillators give pulse shapes that depend on the interacting particle, which allows for the identification of the type of particle that produced a specific pulse. The reason for this is that different particles excite different molecular levels, which have slightly different de-excitation times. This is reflected in the scintillation pulse shapes as shown in Figure 8: the tail of the neutron (proton) pulse shapes is longer than the one of the gamma (electron), a difference that can be exploited using various techniques to distinguish between neutron and gamma events.

Several organic liquid scintillator have been developed over the years, but the one that offers the best performance in terms of pulse shape discrimination is the NE213 type (a.k.a. BC-501A or EJ-301 depending on the manufacturer). The NE213 compound is Xylene (C_8H_{10}) and it has a density of 0.874 g/mL [12].

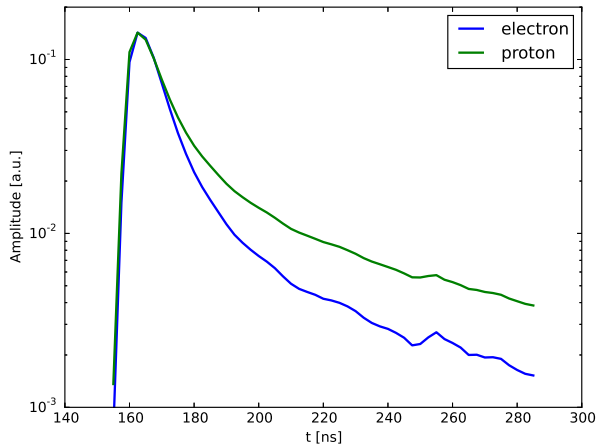


Figure 8: Average proton (neutron) and electron (gamma) pulse shapes for a NE213 liquid scintillator.

It is important to know that the light emission from electron signals is linearly proportional to the energy deposited in the detector (in the energy range interesting for this work), but the same is not true for protons. The non-linearity makes the analysis of neutron pulse height spectra more complicated than that of gammas.

4.5 Comparison between spectrometers

As mentioned before (section 4.1), the quality of a spectrometer can be judged using three properties. Tables 2 and 3 compare the efficiency and resolution of the optimized spectrometers (MPR and TOFOR) with the NE213 for 2.5 and 14 MeV neutrons. Figure 9 shows their response to monoenergetic neutrons. Notice that efficiency, resolution and response do not depend only on the technique but also, to different degrees, on the specific design of the instrument. For example, the MPR employs a flexible system of conversion foils and proton apertures, which makes it possible to vary the performance within certain limits.

In general the resolution of the optimized spectrometers is better than the NE213, while for the efficiency it is the opposite. However one must be careful when talking about efficiency, because the final counting statistics depends also on the active area of the spectrometer (i.e. the area facing the plasma that can detect neutrons), the distance from the plasma and the dimensions of the collimator. In addition, practical aspects like gain stability, count rate capability, robustness etc. will also play a role in any practical implementation of a neutron spectrometer for fusion.

Regarding the neutron response functions, it is clear that the MPR and TOFOR responses are more suitable for spectroscopy because they are peaked, thus more similar to the ideal delta response than the NE213 response, which has a box-like shape, extending up to a certain maximum.

Table 2: Efficiency and resolution of the MPR and NE213 for 14 MeV neutrons.

	MPR	NE213
Efficiency	$0.51 - 11 \cdot 10^{-6}$	~ 0.03
Resolution	1.95 – 4.24 %	$\sim 4\%$

Table 3: Efficiency and resolution of the TOFOR and NE213 for 2.5 MeV neutrons.

	TOFOR	NE213
Efficiency	0.01	~ 0.08
Resolution	7.4 %	$\sim 12\%$

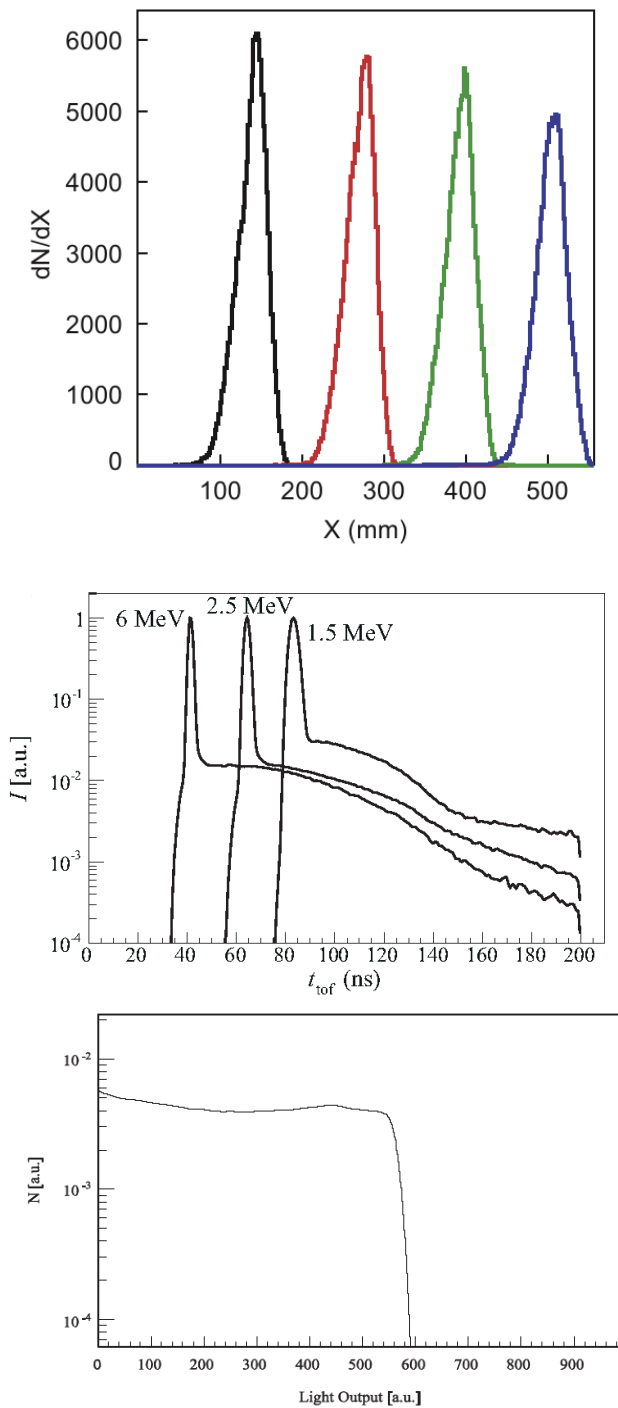


Figure 9: Response of the MPR spectrometer to 12.6 MeV (black), 14.0 MeV (red), 15.4 MeV (green) and 16.8 MeV (blue) neutrons (top); response of the TOFOR spectrometer to three neutron energies (middle); response of the NE213 spectrometer to 14 MeV neutrons (bottom).

5 The “Afterburner” installation

The MPRu spectrometer has a pre-prepared cavity in the back, before the beam dump, where different detectors can be tested. A NE213 liquid scintillator and a diamond detector [13] were installed in this cavity. The NE213 installation was named “Afterburner”, since it measures neutrons after they have gone through the thin conversion foil, as well as the entrance and exit windows of the vacuum chamber of the MPRu. The original idea behind the installation was to allow neutron flux measurements with millisecond time resolution during DD operations, when the low efficiency of the MPRu prevents the time resolution of JET discharges. However in this work it was used to investigate the neutron spectroscopy capabilities of NE213 scintillators.

5.1 Detector specifications and assembly

The detector consists of a cylindrical cell with 12.3 mm diameter and 8.4 mm height, for a total active volume of about 1 cm³. The cell is light coupled to a PMT (Hamamatsu R5611 [14]) and the whole assembly is embedded in an aluminium casing. The PMT is shielded against magnetic fields by a 1 mm thick μ -metal layer. The detector is held in position by a soft iron cylinder which also serves as additional magnetic shielding. Three cables are connected to the PMT: a cable with SHV connector for high voltage supply, a cable with BNC connector to read the signal, and an optical fiber to send external light signals such as LED pulses to the photocathode of the PMT. Figure 10 shows the detector and the holder.

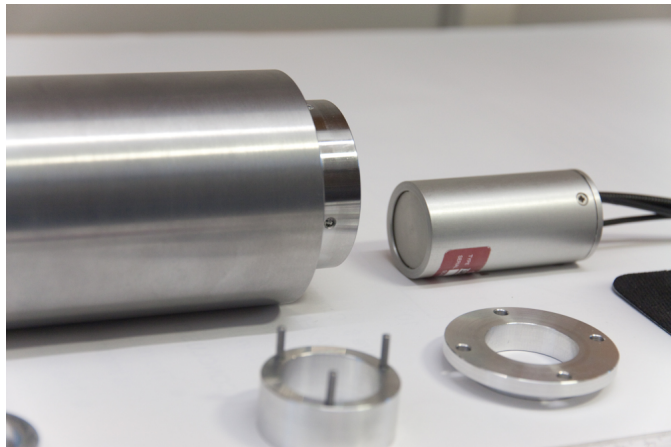


Figure 10: The holder (left) and the Afterburner detector (right).

The holder also keeps a ²²Na gamma source, used for the energy calibration (see section 6.4) and the monitoring of the gain drift of the PMT (see section 8.1.1),

in front of the detector.

The full PMT pulses are recorded digitally using a SP Devices ADQ214 digitizer (14 bit, 400 MSPS) [15] and stored on a local computer.

5.2 Line of sight and Field of view

Figure 11 shows the position of the MPRu and the Afterburner with respect to the JET tokamak.

The line of sight (LOS) of a detector is defined as the line that passes through the center of the detector and the center of the collimator. The field of view (FOW) is instead defined as the set of weights of the contribution to the measurement of each point in the observed volume, independently of the spatial distribution of the actual (neutron) emission from the source. Here we adopt a straight-forward “optical” approach to determine which parts of the plasma volume are actually seen from the detector, as further discussed below.

The Afterburner and the MPRu share the same line of sight, but their fields of view differ because of the different active area (10 cm^2 for the MPRu, 1 cm^2 for the Afterburner) and because of the different distance between the detector and the collimator, as shown in Figure 12.

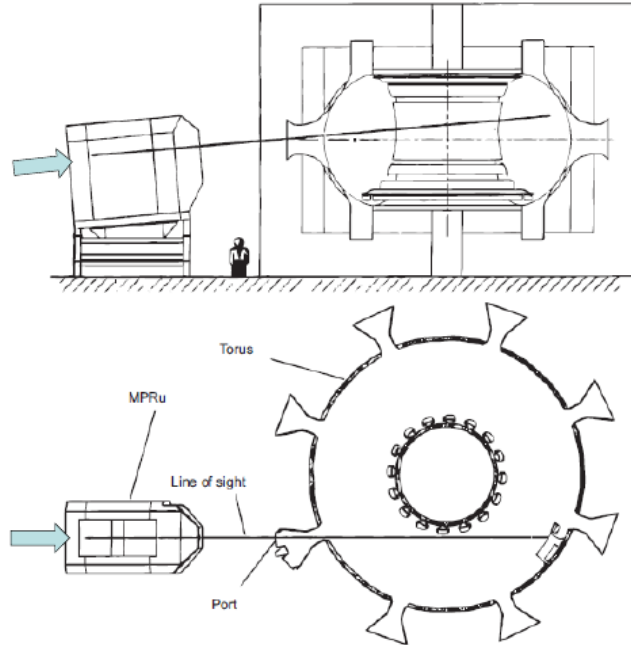


Figure 11: Position of the MPRu inside the JET torus hall. The position of the Afterburner is indicated by the blue arrow.

Most of the time the geometry of the FOW is complicated, so it is not practical to calculate it analytically. Therefore a code named LINE 2 was developed to compute the FOW numerically. It is an optical code: only geometrical effects are considered and no nuclear reactions are involved, therefore the hindering objects are completely opaque and do not let any particle go through. In the input of the code one defines the plasma volume, the detector position and dimensions, and the limiting surfaces, i.e. all the surfaces that prevent the neutrons from reaching the detector surface, such as the front of the collimator. The code divides the plasma volume in voxels and calculates the solid angle constituted by the detector as seen from each of these voxels using numerical methods. The weight is then the product of the volume of the voxel times the solid angle.

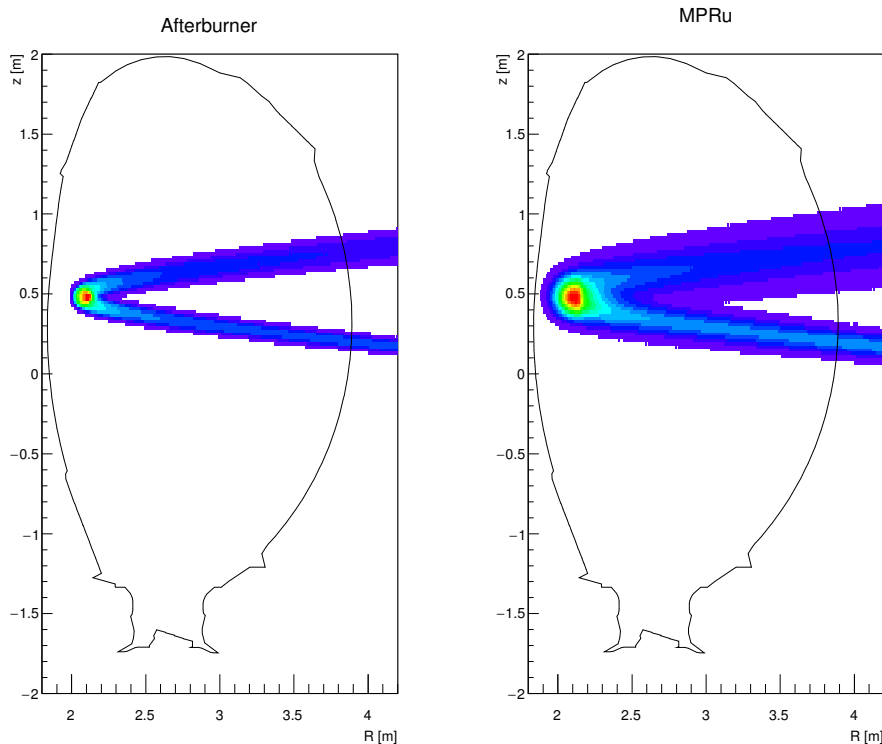


Figure 12: Poloidal projection of the FOW of the Afterburner (left) and the MPRu (right). The colour is proportional to the sum of the weights of the voxels with coordinates (z, R) .

6 Afterburner system characterization

6.1 Typical pulses

Figure 13 shows examples of pulse shapes recorded with the Afterburner. There are three different processes that produce signals in the detector: gamma, neutron and LED induced events. Technical issues that still need to be investigated prevented the collection of LED signals during the JET experiments used in this work.

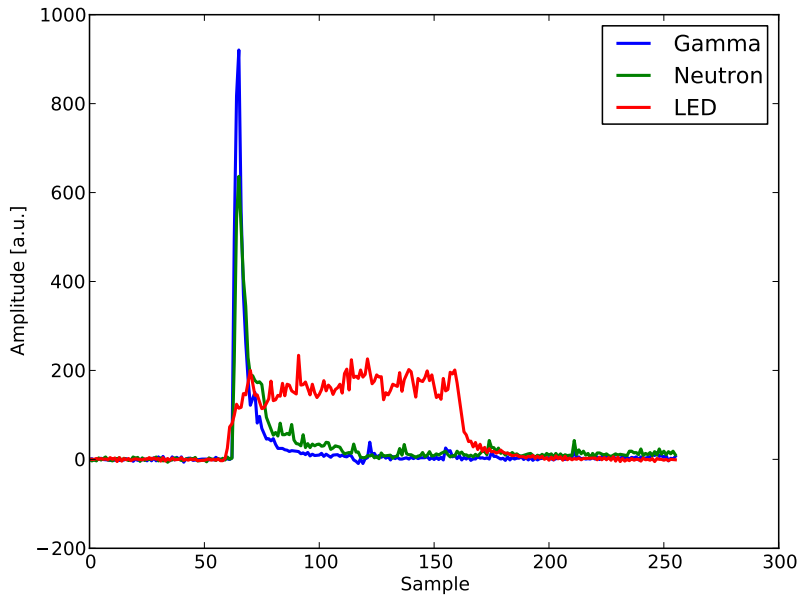


Figure 13: Typical Afterburner scintillation pulses produced by gammas (blue), neutrons (green) and LED signals(red).

6.2 Pulse shape discrimination

As shown in Figure 8, it is possible with NE213 scintillators to distinguish between gamma and neutron induced signals, thanks to the difference in pulse shape. There are many practical ways of doing that, but the one that was chosen for the Afterburner is the charge comparison method. It consists in integrating the pulses in different integration intervals, a short one and a long one, as shown in Figure 14. The integration over the long gate gives the total charge of the pulse (Q_{tot}), while the integration over the short gate gives the short charge (Q_{short}). The factor used for pulse shape discrimination (PSD) is given by:

$$PSD = \frac{Q_{tot} - Q_{short}}{Q_{tot}}. \quad (8)$$

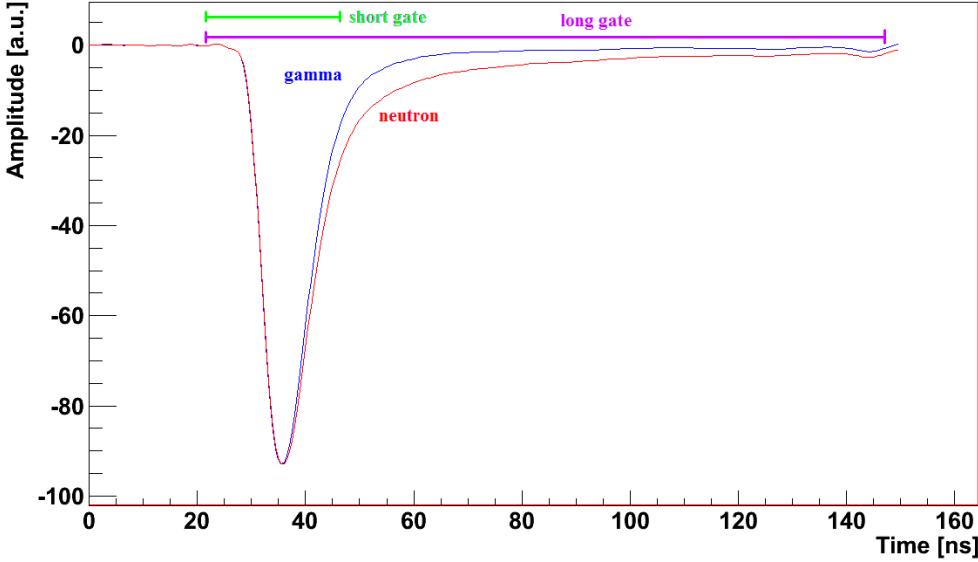


Figure 14: Integration gates used for pulse shape discrimination.

Since the neutrons have a more pronounced tail, the value of PSD for neutron events will be higher than the one for gamma events. The recorded events can then be collected in a 2D histogram, as shown in Figure 15, so that it is possible through appropriately chosen cuts to separate gamma and neutron events.

The quality of the PSD depends on the particle energy, being worse at low energies. It can be assessed by taking the 1D projection of the PSD histogram on the y axis, within a selected total charge interval, and then calculating the following figure of merit (FOM):

$$FOM = \frac{\Delta PEAK}{FWHM_\gamma + FWHM_n}, \quad (9)$$

where $FWHM$ stands for full width at half maximum and $\Delta PEAK$ is the distance between the gamma and the neutron peaks, as illustrated in Figure 16.

The FOM values for some total charge intervals for Afterburner data from JET discharge 86459 are shown in Table 4.

The FOM allows to compare the PSD performance of different detectors and different PSD methods, but also allows to find the integration gates for the charge

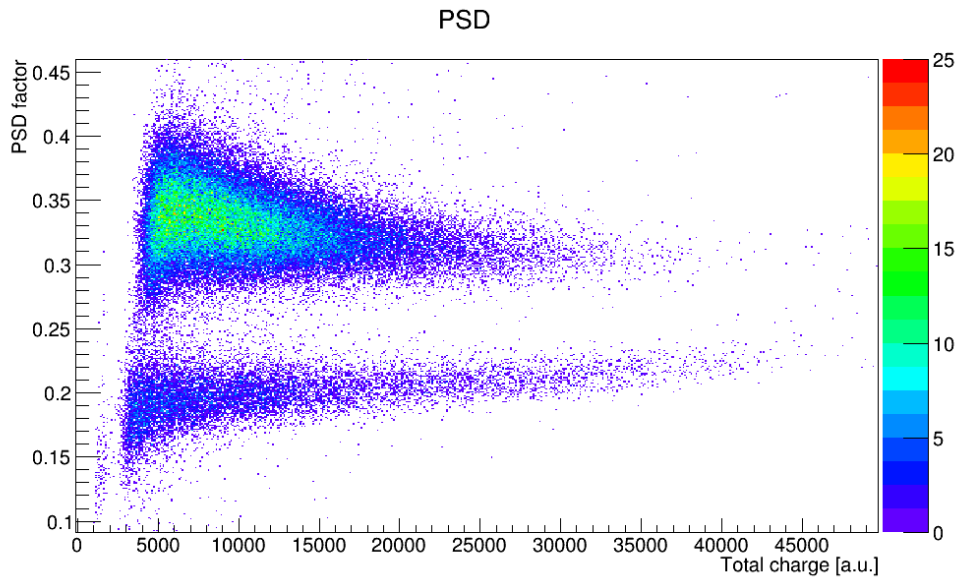


Figure 15: 2D histogram for pulse shape discrimination.

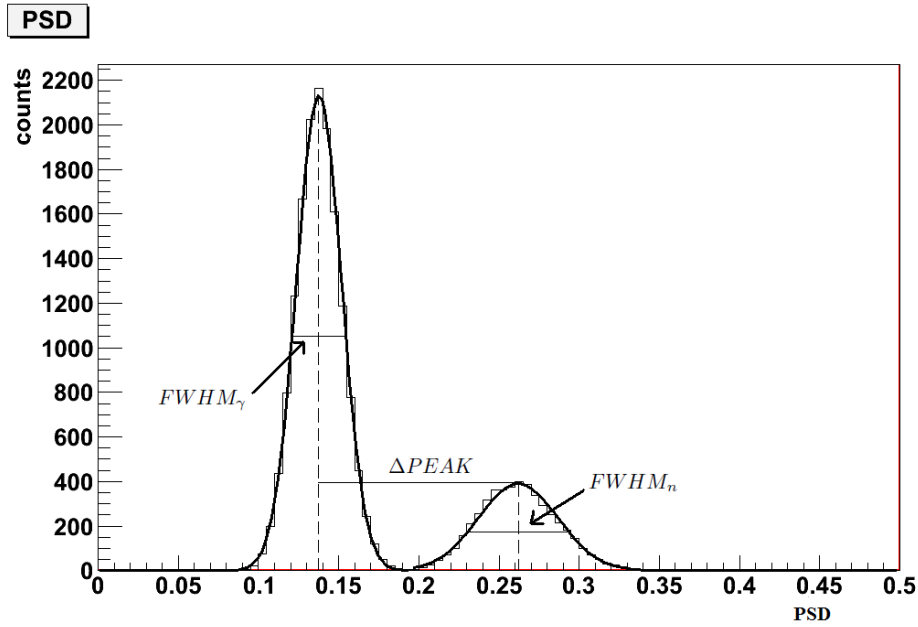


Figure 16: Illustration of the components in the FOM calculation. 1D projection of a slice of the PSD histogram on the y axis.

integration that give the best PSD. The values given in Table 4 were obtained with the integration gates that give the highest FOM in the present study.

Table 4: FOM values for the Afterburner data from JPN 86459.

	$5k < Q_{tot} < 10k$	$10k < Q_{tot} < 15k$	$15k < Q_{tot} < 20k$
FOM	2.25	2.33	2.35

6.3 MCNPX model

In order to properly interpret the measured PHS it is necessary to know the detector response to both gammas and neutrons. The response can be computed by numerical simulations using a MCNPX model of the detector [16]. Figure 17 shows the geometry of the model, which includes the whole MPRu spectrometer with its concrete shielding.

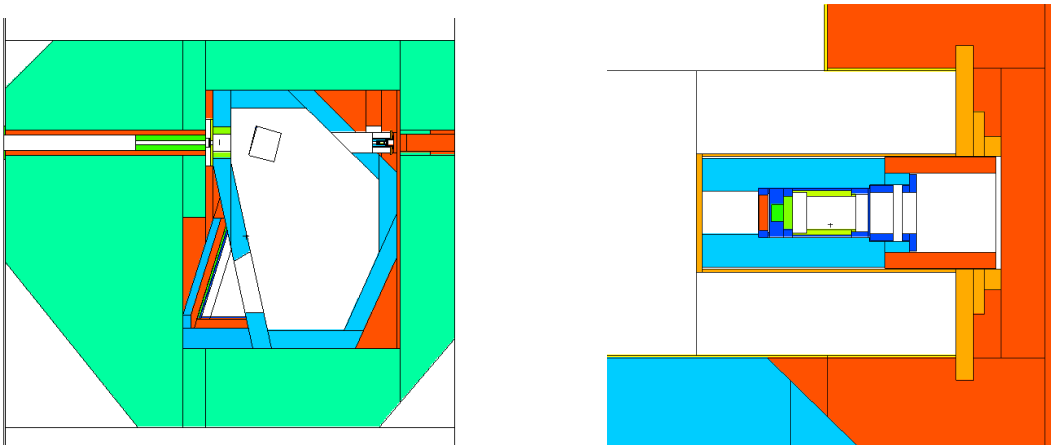


Figure 17: Geometry of the MCNPX model of the MPRu and Afterburner; overview (left) and close view on the Afterburner (right).

The response to gammas is calculated only at the energies of emission of the ^{22}Na gamma source: 511 keV and 1275 keV. The two energies are simulated separately. In the simulation the gamma particles are emitted isotropically from the position where the source is located. The energy deposited in the scintillator is recorded in a histogram which represents the response of the detector. Figure 18 shows the calculated response to the two gamma energies.

For the response to neutrons the process is similar, but since the distribution of energies of the neutrons that are expected to impinge on the detector are not known a priori and change depending on the plasma conditions, a response matrix is built simulating monoenergetic neutrons from 1 to 7 MeV with 50 keV steps. The neutrons are generated uniformly from a disk source placed at the front of the neutron collimator, with direction parallel to the axis of the collimator. The radius of the disk source is slightly bigger than the radius of the collimator entrance.

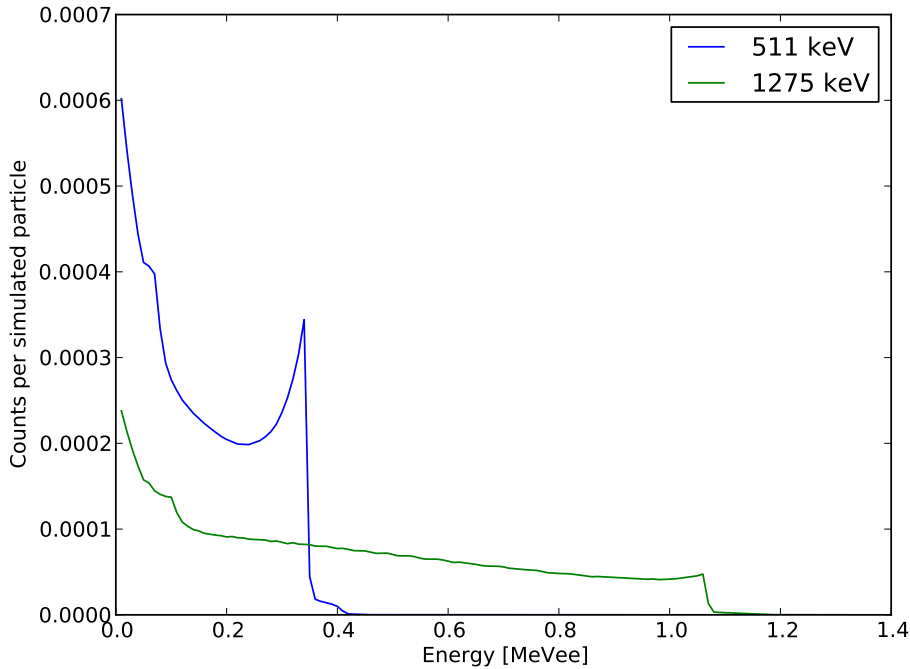


Figure 18: Response of the Afterburner detector to the gamma energies emitted by a ^{22}Na source calculated with MCNPX.

Each of the rows of the matrix is a PHS obtained from a monoenergetic neutron. This way the expected PHS from a certain neutron spectrum can be obtained by multiplying the neutron spectrum with the response matrix:

$$M_j = NRM_{i,j} \cdot S_i, \quad (10)$$

where M is the estimated PHS, NRM is the neutron response matrix, S is the neutron spectrum, the subscript j represents the light yield i represents the neutron energy.

The simulation of the neutron response is more complicated because of the fact that the proton light yield of NE213 scintillators is not linear (see section 4.4.1). MCNPX allows the user to introduce a non-linear light yield function in order to get the proper intensity of the scintillation light in the detector. The scintillation light from scattering on carbon is not included in the calculation. However this is not a problem if the analysis of the PHS is performed with a energy threshold high enough, since the intensity of the light produced by recoil carbon is low compared to that produced by protons. For neutron energies above 7 MeV one needs to include the effect of other, inelastic, reactions on carbon in the calculation, as

explained in section 4.4.1.

Figure 19 shows the calculated response of the Afterburner to some neutron energies.

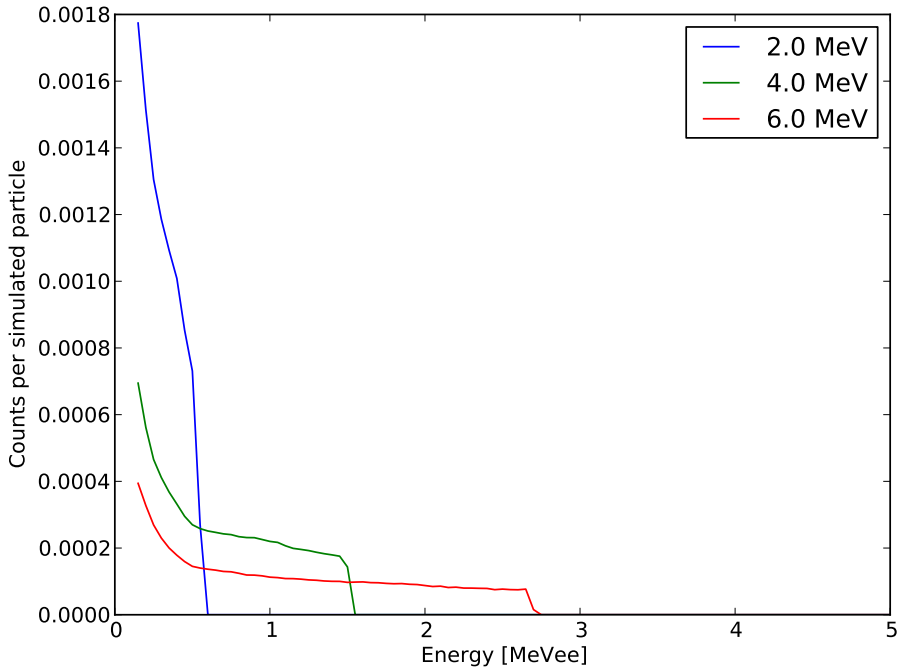


Figure 19: Response of the Afterburner detector to monoenergetic neutrons of 2 (blue) 4 (green) and 6 (ref) MeV calculated with MCNPX.

6.4 Gamma and neutron calibration

The MCNPX simulation does not include the resolution of the detector, nor the conversion factor between light output, which is given in electronvolt electron equivalent (eVee) units, and the total charge obtained in the integration of the measured pulses. The resolution can be added to the simulated response by substituting each point with a gaussian with FWHM given by equation 7. The relationship between eVee and total charge is linear (in the energy region of interest), thus can be described by the simple equation:

$$E[keVee] = k \cdot Q_{tot} + m. \quad (11)$$

The three resolution parameters α , β , γ of equation 7 and the two calibration parameters k and m are not known a priori, but they can be obtained from a

fit of the well known ^{22}Na gamma spectrum measured with the detector. As mentioned before, the ^{22}Na source produces 2 gamma lines. Each of them carries information about the calibration (through the position of the Compton edge) and the resolution (through the broadening of the Compton edge), hence there are 4 “information points” in the ^{22}Na spectrum. To overcome the problem that there are only 4 points for 5 fitting parameters, the PHS of neutrons emitted from ohmically heated plasmas can be used as a known spectrum for calibration. It can be demonstrated that the neutron spectrum from ohmic plasmas is a Gaussian distribution with broadening proportional to the square root of the ion temperature [7]. At JET the ion temperature for ohmic plasma discharges is about 2 keV.

With the ohmic spectrum we are adding two extra “information points” (The position of the edge of the spectrum and its broadening), giving 6 in total for 5 fitting parameters. We can therefore add a sixth parameter that we call k_n . It is a parameter that we apply to the neutron response matrix only, as a multiplication factor to the light output axis of the matrix. For instance, if $k_n = 0.5$ the column in the response matrix that originally corresponded to 1 MeVee will become 0.5 MeVee. The reason for this addition is the fact that there is no measurement of the proton light yield of the detector, therefore a standard light yield function from literature needs to be assumed for the MCNPX calculation of the response. The k_n factor introduces a correction to this assumption.

The evaluation of the parameters is done iteratively with the following steps:

1. fit gamma PHS with α, γ, k, m as free parameters (β fixed);
2. fit neutron PHS with k_n, β as free parameters (α, γ, k, m fixed).

After some iterations the value of the parameters converges. In this study, the parameter α converges to zero, probably because the small dimensions of the detector make the light collection fairly uniform. This simplifies the calibration processes, since it is possible to assume $\alpha = 0$ and the gamma and neutron calibration can be performed separately without iteration.

Figure 20 shows a fit of the ^{22}Na gamma PHS and Figure 21 shows a fit of the ohmic neutron PHS. The ohmic spectrum includes two components, the direct spectrum and the backscatter. For the direct spectrum an ion temperature of 2 keV was assumed. The evaluation of the backscatter component will be described in section 8.2.1. The ohmic PHS is the sum of the ohmic part of about 650 JET discharges from campaign C33 (from JPN 84743 to JPN 85396).

The results of the calibration for the data from the JET experimental campaign C33 are shown in Table 5.

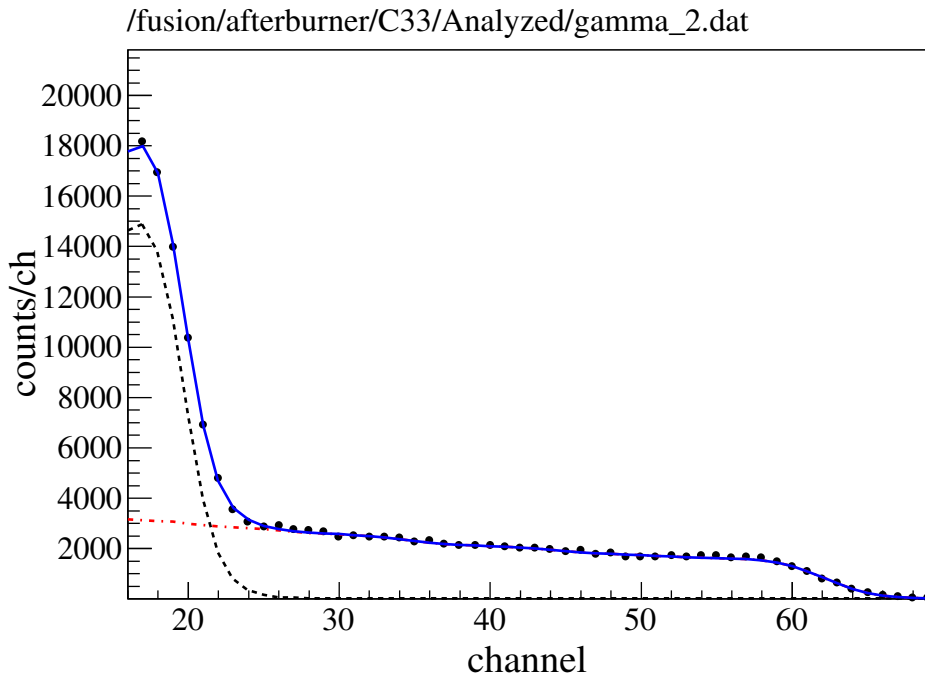


Figure 20: Example of a fit of a ^{22}Na gamma spectrum measured with the Afterburner. The points are the measured data, The black dashed line is the 511 keV component, the red dash-dotted line is the 1275 keV component and the the blue line is the sum of the two.

Table 5: Resolution and calibration parameters for the data from JET campaign C33.

Parameter	Value	Uncertainty
α	0	N.A.
β	8.76	0.26
γ	4.53	0.20
$k[\text{keVee}/\text{channel}]$	16.939	0.010
$m[\text{keVee}]$	17.58	0.22
k_n	0.967	0.002

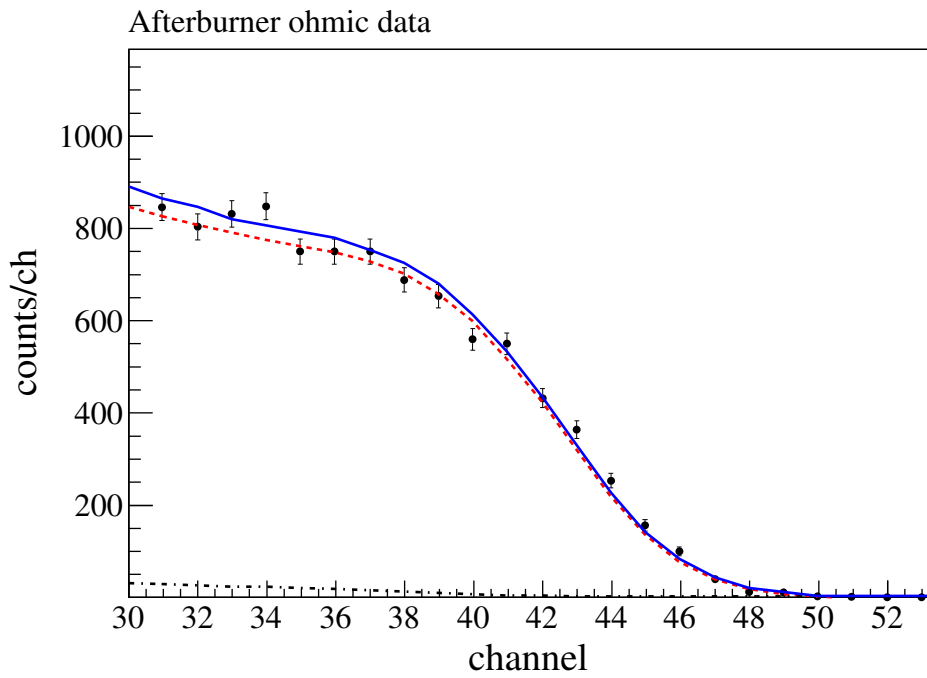


Figure 21: Fit of the ohmic data from campaign C33. The total spectrum (blue solid) is composed of two components: the direct spectrum (red dashed) and the backscatter (black dot-dashed).

7 Dacsim - Data acquisition chain simulation (Paper I)

Understanding the effect of the acquisition chain (PMT, cable, digitizer) on the conversion of scintillation light into an electric signal can help in the evaluation of the performance of a system. The Dacsim (Data acquisition chain simulation) code was developed for this purpose [17] [18].

7.1 The code

The starting assumption is that each event deposits a certain amount of energy (in MeVee) in the scintillator. The energy distribution of the events can be chosen arbitrarily with an input file.

The energy is converted into a number of photo-electrons which is Poisson distributed, with the average number being proportional to the deposited energy. The proportionality factor is the product of the energy conversion factor (photons/MeVee), the quantum efficiency of the photocathode, and the light collection efficiency. The quantum efficiency and the light collection are assumed to be constant in space, while in reality they can change depending on the position of energy deposition. The photo-electrons are then spread in time according to an exponential decay function composed of three decay times, which correspond to different molecular excitation levels. As explained in section 4.4.1 electrons and protons excite different molecular levels, therefore their signal's decay times are different, and this is considered in the code.

The multiplication in the PMT is a Poisson process in which the variance is dominated by the first dynode in the chain [10]. This is implemented in the code by producing a multiplication factor for each of the photo-electrons which is proportional to the overall gain but has a relative variance given by:

$$\frac{\sigma_{gain}^2}{gain} = \frac{1}{\delta - 1}, \quad (12)$$

where δ is the multiplication factor of a single dynode. The signal is then convolved with a Gaussian that simulates the PMT time response.

The cable filters low frequencies in the signal, and the level of attenuation depends on the type and the length of the cable. In the code the cable is modeled as a simple low-pass filter for which it is possible to select the cut-off frequency. Electric noise is also added as random Gaussian oscillations on the signal. The intensity of the noise can be chosen in the input file.

Finally the digitizer simply samples the signal with a given sampling frequency and resolution.

The code can also simulate pile-up, by generating a series of random trigger time intervals according to the count rate, which can be chosen in the input file. When the time interval is shorter than the total pulse length, the corresponding events are added up, simulating a pile-up event. The addition is performed before the PMT response is added.

7.2 Examples

An example of the average pulses generated by the code compared to pulses measured by the Afterburner is shown in Figure 22.

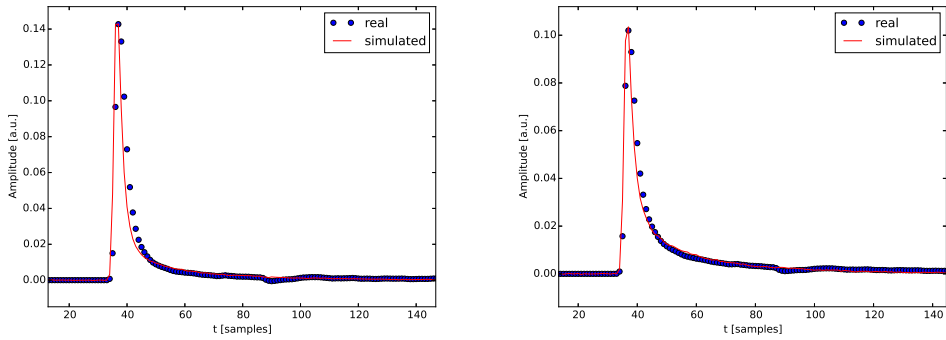


Figure 22: Comparison between the average gamma (left) and neutron (right) pulses from the Afterburner (blue dots) and from the Dacsim code (red line). The code input was set-up to obtain a good match with the real pulses.

One can use the code for example to study the effect of the data acquisition chain on the pulse shape discrimination. Figure 23 shows simulated PSD plots without and with pile-up.

The code was used to evaluate the goodness of the pile-up rejection method used for the Afterburner. The results of the evaluation are presented in section 8.1.2.

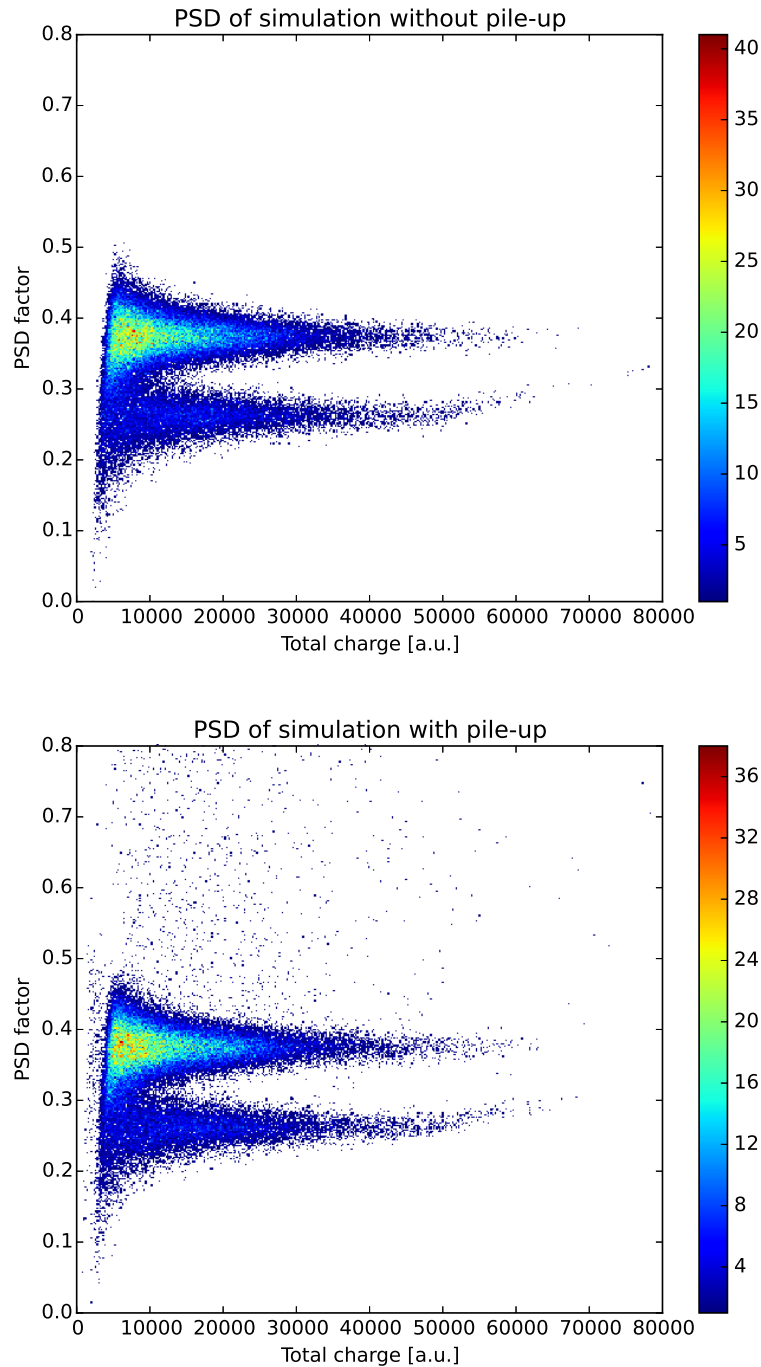


Figure 23: Pulse shape discrimination plots of the simulated pulses without pile-up (top) and with pile-up (bottom).

8 Data analysis

8.1 Data processing

Before the actual spectroscopic analysis, the data need to be treated to account for two effects: gain drift and pile-up.

8.1.1 Gain drift

Gain drifts are changes in the gain of the PM tube. It is convenient to classify gain drifts according to the time scale during which they occur: long term (\sim days) and short term (\sim milliseconds).

The long term gain drifts are caused by temperature changes and deterioration of the tube. A reliable way to measure long term gain drifts is to perform periodical measurements of the gamma spectrum from a calibration source and from that calculate the calibration parameters (as shown in section 6.4). This has been done for the Afterburner system on a daily basis during the JET campaigns.

The calibration parameter that is related to the gain is the coefficient k . Figure 24 shows the daily variation of this coefficient during the C33 campaign at JET. It can be noticed that there was a clear deterioration of the gain in the first half of the experimental period, reflected in the plot as an increase in the coefficient k .

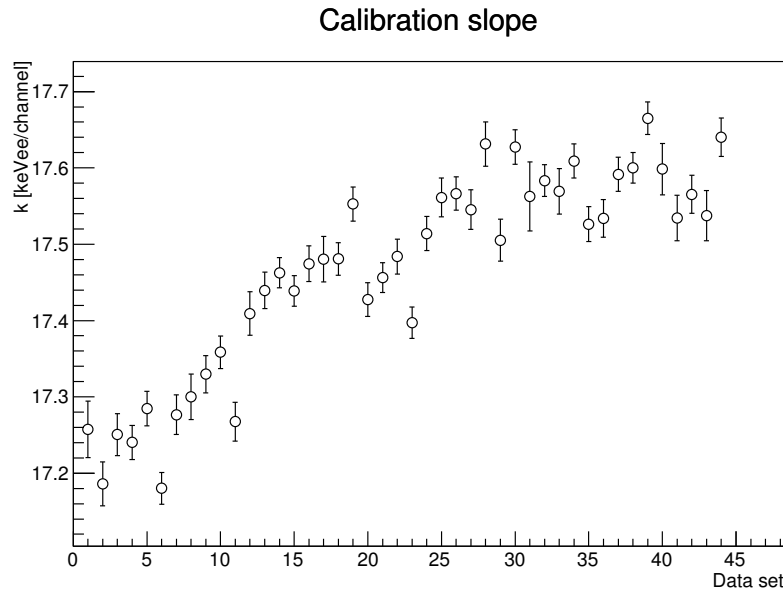


Figure 24: Variation of the calibration parameter k during the C33 campaign at JET. The parameter is inversely proportional to the gain of the PMT.

The correction procedure is straightforward. First one chooses a reference day. Then the total charge of any other day is rescaled to restore the reference calibration, using the formula:

$$Q'_{tot} = \frac{Q_{tot} \cdot k + (m - m_{ref})}{k_{ref}}. \quad (13)$$

The short term gain drifts are caused by high count rates, which produce a current in the PMT that is comparable to the current in the voltage divider circuit. The gain drift is obtained from the formula [19]:

$$\frac{\Delta G}{G} = \alpha \frac{N}{N+1} \frac{I_a}{I_p}, \quad (14)$$

where G is the gain, N is the number of dynode stages in the PMT, I_a is the anode current. I_p is the current flowing in the voltage divider circuit of the PMT, and α is a constant.

Equation 14 implies that the gain increases linearly with the anode current, which in turn is linearly proportional to the count rate in the detector. However when the ratio I_a/I_p approaches 1, the equation does not hold since the anode current is so high that space charge starts influencing the electron trajectories, making the collection efficiency drop drastically. Consequently the gain decreases quickly too.

One way to monitor the short term gain drift is to shine a LED signal into the PMT and monitor the variations in its total charge. If the LED generator is stable enough the only factor affecting the total charge is the gain of the PMT.

The Afterburner is equipped with a LED generator, but technical issues prevented the collection of LED signals during the period of JET campaigns used in this work. In order to obtain an estimate of the gain correction required, LED data from another experiment was used, namely from the NE213 detectors of the MAST neutron camera [20]. These detectors are also NE213 connected to exactly the same kind of PMT as the Afterburner, and with a similar high voltage level applied. Furthermore the average amplitude of the pulses recorded by the MAST detectors is similar to the average amplitude of the Afterburner pulses. Therefore it was possible to use the gain variation as function of count rate in the MAST detectors as an estimate of the gain variation versus count rate in the Afterburner.

The relative variation of the LED total charge vs count rate in the MAST detectors is shown in Figure 25. The count rate in the Afterburner during JET campaign C33 did not exceed 100 kHz, therefore the maximum gain variation is expected to stay within a few percent.

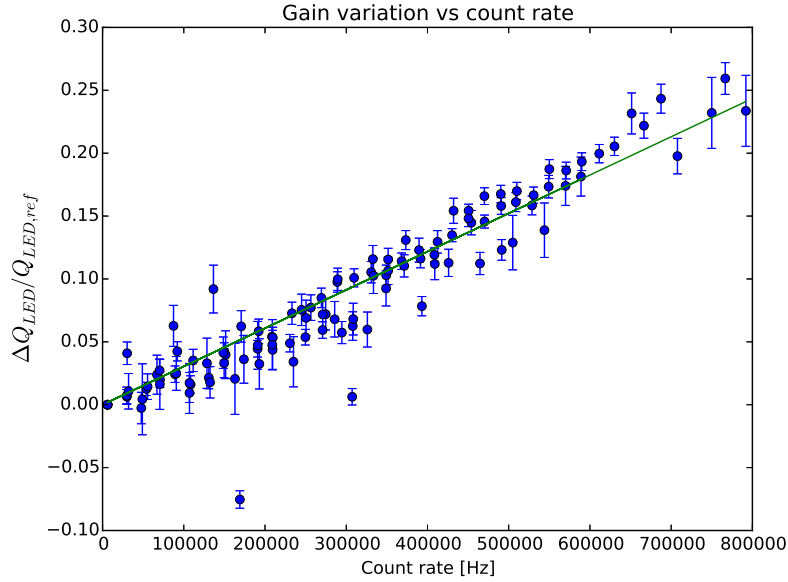


Figure 25: Relative variation of the LED total charge vs count rate in the MAST detectors.

8.1.2 Pile-up rejection

Pile-up occurs when two or more events happen in a time interval shorter than the length of a single event. If not treated properly, pile-up can lead to errors in the evaluation of the total charge of the events.

In this work pile-up events were rejected applying cuts in the PSD plot as shown in Figure 26. This simple method was proven to be applicable using the simulation code described in chapter 7. The code was set up to resemble the experimental conditions of the Afterburner in terms of pulse shapes, energy distribution of the events and count rate. Two simulations, one with and one without pile-up, were compared (Figure 27). A Kolmogorov-Smirnov test of the two distributions (with $Q_{tot} > 10000$) gave 81% probability of the two data sets being sampled from the same distribution, therefore we can safely assume that the two distributions are equivalent.

8.2 Analysis of the neutron pulse height spectra

The strategy for the NES analysis is to model the ion distribution, use it to calculate the neutron emission, fold the resulting neutron spectrum with the response of the instrument (equation 10) and compare the final result with the experimental measurement. In some cases the modeled neutron spectrum depends on some

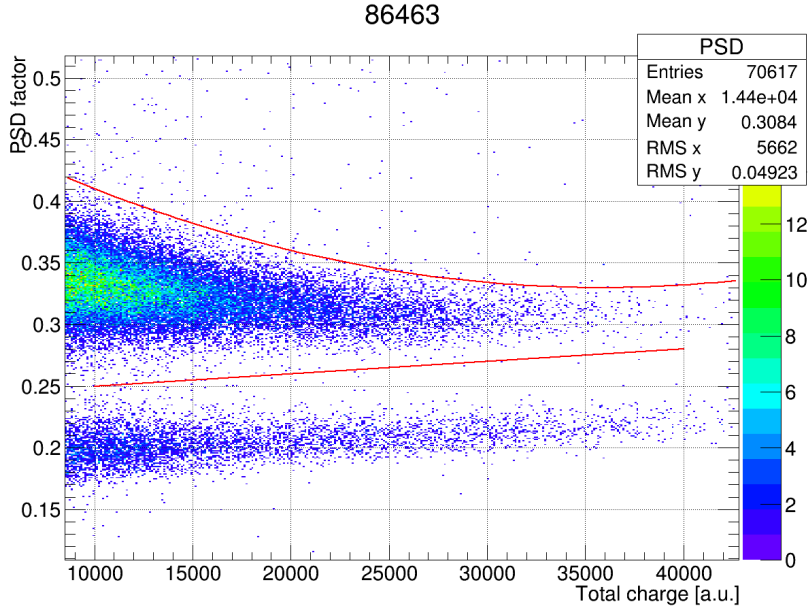


Figure 26: PSD plot for JPN 86463. The cuts applied are shown in red. The events above the neutron cluster are rejected as pile-up events.

parameters that can be fitted to match the data. This analysis strategy is usually referred to as forward folding or forward fitting.

As explained in section 3.1 the neutron spectrum can be divided into spectral components. These components can be kept separated in the analysis and they can then be fitted independently to the data. This way the intensities of the components can be fitting parameters.

An extra spectral component which is present for any plasma condition is the backscatter component. Backscattered neutrons are neutrons that are reflected by the tokamak wall opposite to the spectrometer as seen in the FOW of the spectrometer. Their energy distribution depends on the original energy distribution of the neutrons and on the wall materials. To estimate the backscatter component a backscatter matrix is generated with MCNPX simulations with monoenergetic neutrons. This matrix is an actual response matrix: given the direct neutron spectrum emitted by the plasma one can obtain the expected backscatter spectrum at the detector position by folding the direct spectrum with the backscatter matrix, similarly to what is done in equation 10.

The statistical error in the estimate of the fitting parameters is obtained by sampling randomly the chi-square probability space independently for each of them. The contribution of the calibration parameters to the systematic uncertainty is estimated by varying separately each of them by $\pm\sigma$ and performing the fit again.

The difference between the values of the fitted parameters with unchanged and changed calibration parameter is the contribution of that calibration parameter to the uncertainty.

8.2.1 Thermal fraction estimate (Paper II)

The ratio between the intensity of the thermal component of the neutron spectrum and the total direct spectrum is referred to as the thermal fraction and it is a way to evaluate how much the plasma relies on external heating.

In the NE213 PHS the difference between a purely thermal (ohmic) plasma and a plasma with NBI heating is not very pronounced, but it is clearly visible (Figure 28). The tail in the NBI heated spectrum is slightly more pronounced because of the presence of a beam-thermal component, a fact that points to the possibility to separate the spectral components.

Some JET pulses from campaigns C31 and C32 were selected to study the possibility to use NE213 detectors in the thermal fraction estimate. The criteria for pulse and time slice selection were:

1. NBI is the only additional heating in the pulse;

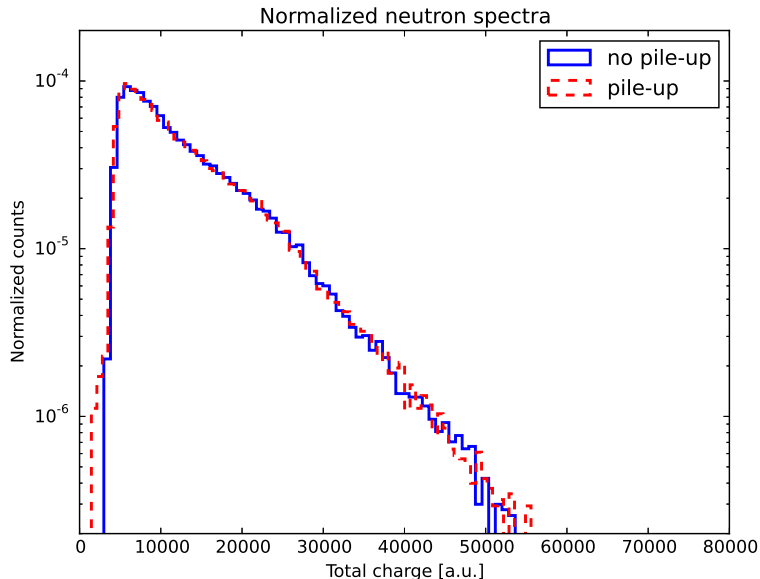


Figure 27: Comparison of the simulated neutron PHS without pile-up (blue solid) and with pile-up after the applications of the same cuts as in the real data (red dashed).

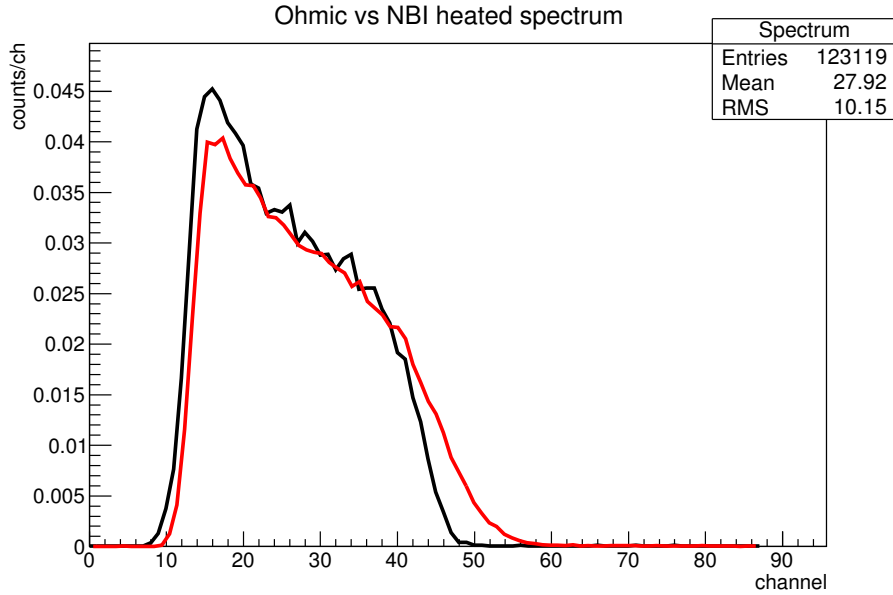


Figure 28: Normalized neutron PHS measured by the Afterburner during ohmic JET discharges (black) and during NBI heated discharges (red). The NBI heated spectrum has a slightly longer tail.

2. The relevant plasma parameters (electron temperature, electron density, neutron yield, Z_{eff} ¹) measured by other JET official diagnostics in the selected time interval are stable;
3. high electron density ($n_e \sim 10^{20} m^{-3}$) so that the beam-beam component is negligible, and $T_i \approx T_e$ can be assumed.

Furthermore the selected discharges needed to cover a relatively wide range of thermal fraction values.

The ion velocity distributions for the pulses were obtained from simulations with the TRANSP code [21]. The components of the neutron spectrum in the Afterburner FOW were then obtained applying the ControlRoom code [22] to the distributions from TRANSP.

The free parameters in the fit were the intensities of the components and the ion temperature, for which the measurement of the electron temperature was set as a Bayesian prior (assuming a relative uncertainty of 10% on the T_e measurement).

For the analysis of the PHS a first fit of the data without the backscatter component is performed; then the result of this fit is folded with the backscatter matrix

¹The effective ion charge is defined as $Z_{eff} = \frac{\sum_i n_j Z_j^2}{\sum_i n_j Z_j}$, where j denotes the ion species in the plasma, n is the density, Z is the charge.

to obtain the backscatter component; finally the backscatter component is added to the spectrum and a new fit is performed.

It is very important to consider the fact that the neutron spectrum and the backscatter matrix depend on the FOW of the instrument. To take that into account the result of the LINE 2 code is included as an input of the code that performs the calculation of the spectral component.

Figure 29 shows the time evolution of the most important parameters of JET pulse number 84866. Figure 30 shows the results of the fit of pulse 84866 in the time interval $t = 55 - 58\text{s}$ for the Afterburner and TOFOR. The Afterburner data start from channel 30 for many reasons: avoiding the modeling of the threshold, avoiding the region where the PSD is not so good, avoiding the region where the light yield from carbon needs to be included in the calculation of the response matrix. The data are fitted only up to channel 60 to avoid the inclusion of empty bins.

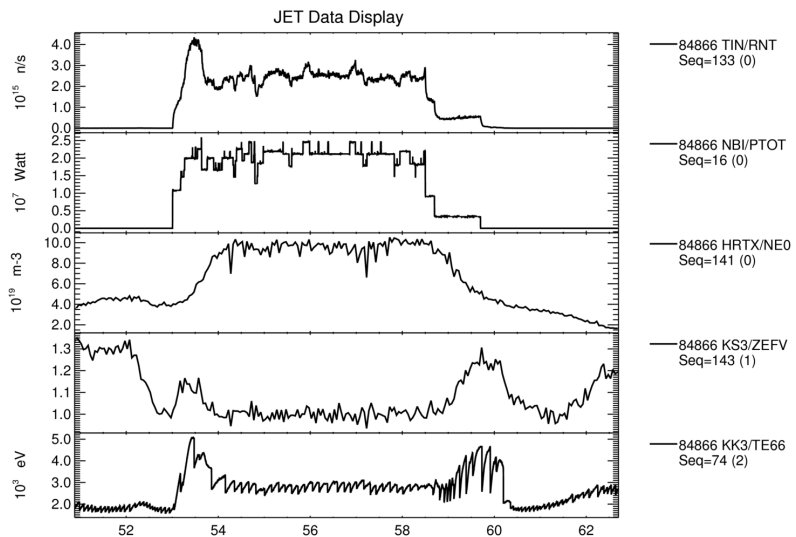


Figure 29: Time evolution of the most important parameters for JPN 84866. From top: total neutron yield; total NBI power; electron density in the core; Z_{eff} ; electron temperature in the core.

The estimates of the thermal fraction for the selected pulses are summarized in Table 6 together with the estimated statistical and systematic errors.

Figure 31 shows the comparison between the Afterburner and the TOFOR thermal fraction estimate. In the plot the correlation between the two is clear; however

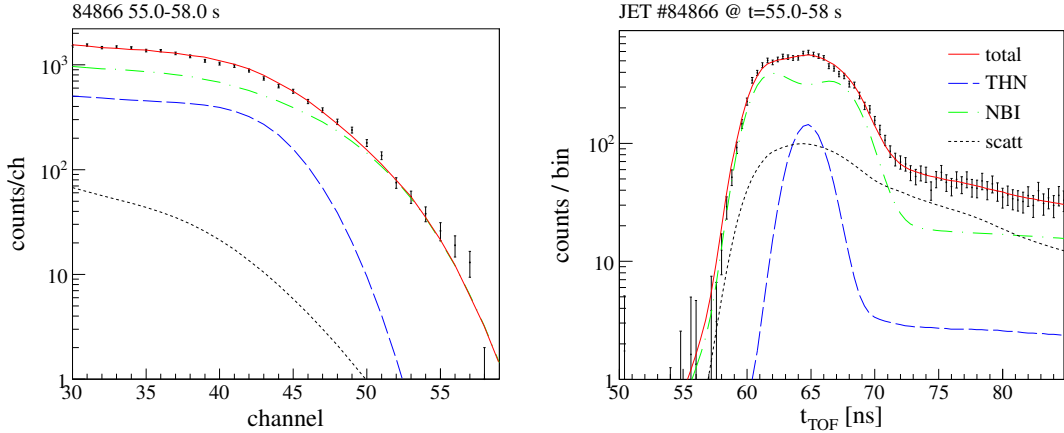


Figure 30: Fit of the Afterburner (left) and TOFOR (right) data for JPN 84866.

The only additional heating was NBI. The components of the neutron spectrum are: thermal-thermal (THN), beam-thermal (NBI) and backscatter (scatt).

it is also clear that there is a bias in the comparison, since the Afterburner estimate is systematically higher than the TOFOR estimate. This might be explained by the fact that plasma rotation, which would affect the neutron spectrum along the Afterburner LOS but not the one along the TOFOR LOS, was not included in the neutron emission model. It should also be noted that the uncertainties in the results from the Afterburner are 4 to 7 times higher than those from TOFOR.

Table 6: Results of the thermal fraction analysis. The columns, from left to right, are:
JET pulse number; selected time interval in the JET pulse; TOFOR estimate of the thermal fraction; Afterburner estimate of the thermal fraction; statistical uncertainty on the Afterburner estimate; negative systematic uncertainty on the Afterburner estimate; positive systematic uncertainty on the Afterburner estimate.

Discharge #	Δt (s)	$\frac{I_{th}}{I_{tot}}$ (TOFOR)	$\frac{I_{th}}{I_{tot}}$ (Afterburner)	σ_{stat}	σ_{sys}^-	σ_{sys}^+
84866	55.0 – 58.0	0.087 ± 0.012	0.227	0.025	0.030	0.045
84886	50.5 – 52.5	0.247 ± 0.017	0.378	0.028	0.036	0.048
84889	52.0 – 55.0	0.273 ± 0.014	0.419	0.023	0.031	0.036
84976	49.0 – 51.0	0.196 ± 0.016	0.285	0.029	0.031	0.081
84976	53.6 – 55.6	0.0	0.131	0.050	0.030	0.019
85387	57.0 – 59.0	0.136 ± 0.013	0.161	0.030	0.006	0.072

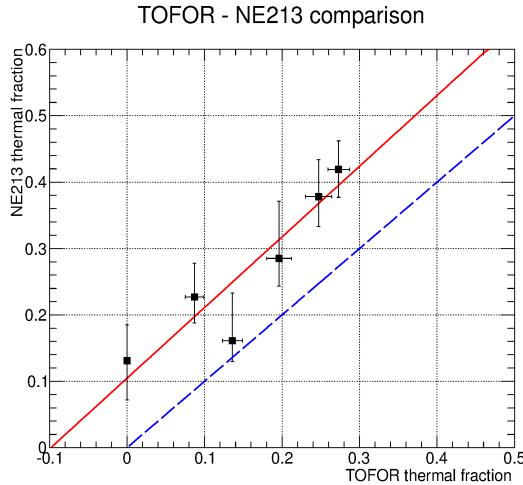


Figure 31: Comparison between the Afterburner and the TOFOR estimates of the thermal fraction. The red solid line represents the best linear fit; the blue dashed line represents the ideal 1 to 1 relationship. Reprinted with permission from Rev. Sci. Instrum. 85, 11E123 (2014). Copyright 2014, AIP Publishing LLC.

8.2.2 Third harmonic radio-frequency heating analysis (Paper III)

Third harmonic radio-frequency (RF) heating is a type of ICR heating that, as the name says, exploits the resonance of the 3rd harmonic of the ion cyclotron frequency. This heating scheme, used in combination with NBI heating, produces very energetic fuel ions, and consequently the neutron spectrum presents a distinctive high energy tail, reflecting the high energy tail in the ion distribution. The maximum energy in the ion distribution is inversely proportional to the electron density [23].

The effect can be clearly seen in the NE213 spectra as shown in Figure 32, which also shows that the endpoint of the tail of the spectrum is sensitive to changes in the electron density.

Since the interest here is mainly in the high energy tail, the influence on the PHS from triton burn-up neutrons must be considered. Because of the box-like shape of the neutron response of the NE213 (Figure 19) the 14 MeV neutrons from triton burn-up affect the PHS down to very low energies. The number of counts from TBN is not high, but it can affect the endpoint of the tail of the spectrum, as shown in Figure 33.

The TBN contribution was removed assuming that it produces a flat distribution of events over the entire energy range up to about 4 MeVee. This assumption is not good for low energies, but it holds in the range of energies where we perform the data analysis (above ≈ 1 MeVee). The estimate of the height of this contribution

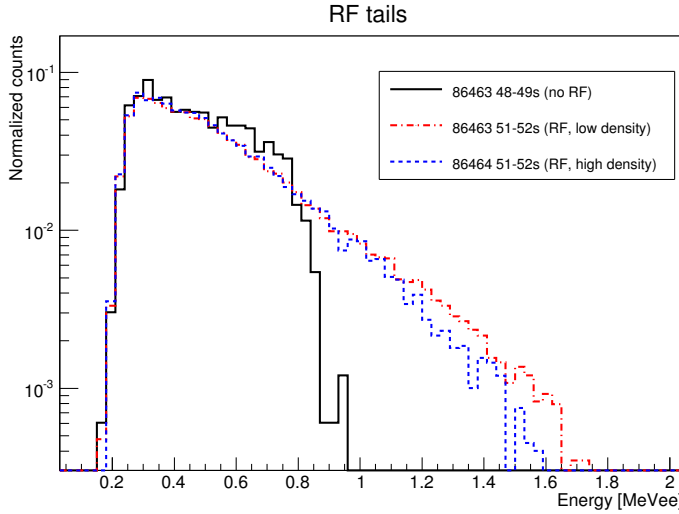


Figure 32: Afterburner neutron PHS for JET discharges with NBI heating only (solid black), with NBI+RF heating and low electron density (dash-dotted red) and with NBI+RF heating and high electron density (dashed blue).

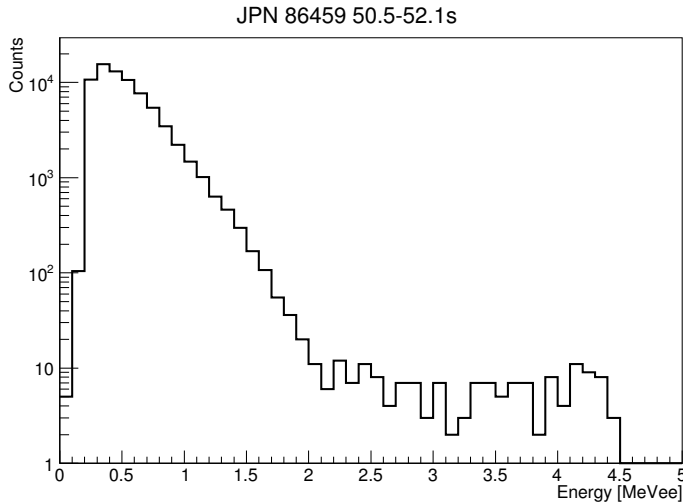


Figure 33: Afterburner neutron PHS for JPN 86459. The plateau from 2 to 4.5 MeVee comes from TBN signals.

was given by the average counts in the PHS bins from 2.4 to 4 MeVee.

Figure 34 shows the comparison between data (after the triton burn-up correction) and the modeled PHS for JET discharges 86459 and 86464. The model used

for the ion distribution is based on a 1D Fokker-Plank model described in [23, 24]. The parameters of the model are optimized to fit the data from TOFOR.

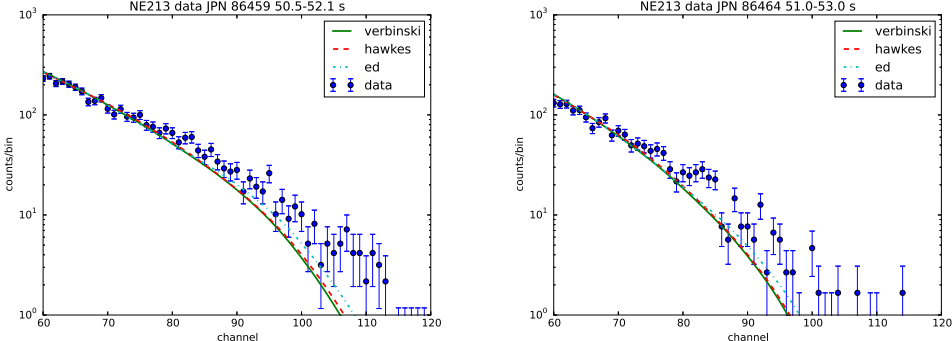


Figure 34: Comparison between the modeled and the measured neutron PHS for JPN 86459 and 86464.

Fig. 34 also shows results from an assessment of the impact of using different proton light yield functions from literature in the analysis. Three different response matrices were produced using different light yield functions [11, 25, 26] and then used separately for the analysis. The chi-square values from the comparisons are summarized in Table 7. The overall agreement is good, but in both discharges it seems that the model underestimates the endpoint of the spectrum. This might be caused by the simplified assumptions used in the modeling of the fuel ion distribution functions in references [23, 24]. In this modeling the pitch angles of the ions (i.e. the angle between the velocity of the ion and the magnetic field) are evenly distributed between 80 and 100 degrees. This assumption does not affect much the resulting spectrum along the TOFOR line of sight, while the spectrum along the Afterburner line of sight is very sensitive to changes in the pitch angle distribution. This indicated that more realistic and detailed models of the fuel ion velocity distributions should be used in future studies of these experiments.

Table 7: reduced chi-square values obtained in the comparison between modeled and measured neutron PHS for JET discharges 86459 and 86464.

	Hawkes	ED	Verbinski
86459	1.95	1.68	2.15
86464	1.67	1.63	1.85

9 Conclusions

The objective of this work is to assess the potential and the limits of the use of NE213 liquid scintillators as neutron spectrometers for fusion plasmas. A NE213 liquid scintillator, the Afterburner, was installed at JET on the same line of sight of the MPRu spectrometer and used to collect data during the JET experimental campaigns to attempt neutron emission spectroscopy analysis.

The understanding of the spectroscopy capabilities of the detector can be achieved only after a proper characterization of the response of the detector, which here was obtained by combining simulations of the system with MCNPX and real measurements. The calibration measurements included data both from a ^{22}Na gamma source and from JET plasma discharges with ohmic heating only.

The Dacsim code was developed to simulate detector pulses including the effect of the components of the data acquisition chain. The code was used to validate the pile-up rejection method used for the data analysis.

Neutron pulse height spectra from NBI heated plasmas were analysed and the thermal fraction in the neutron emission was estimated. The results were compared with the thermal fractions obtained with the TOFOR spectrometer. The estimates from the two instruments showed a clear correlation. The uncertainty on the Afterburner estimates were 4 to 7 times higher than for TOFOR. A systematic bias in the comparison is also present and might be explained by the fact that the instruments have different lines of sight.

The high energy tail of the neutron pulse height spectra from third harmonic RF heated plasmas were compared to the modeled PHS, which was optimized to fit the TOFOR data. The comparison was good but the model gives a slight underestimate of the endpoint of the PHS. This might again be explained by the fact that the different lines of sight are less or more sensitive to different parameters in the model.

The experience gained in this study permits to conclude that NE213 liquid scintillators can provide valuable spectroscopic information, but the quality of the results is far from the more complex instruments such as TOFOR, which are optimized for neutron spectroscopy.

Acknowledgments

Many people deserve to be thanked for many reasons.

Göran, thanks for being such a wise mentor. Thanks Erik and Carl for all the scientific input you give to my work. Thanks Jacob and Sean for providing constant supervision, despite not being officially listed as supervisors.

Thanks to the other colleagues of the Fusion group (present and past): Anders, Iwona, Marco, Mateusz, Matthias, Natalia, Siri. All of you make/made my working time a real pleasure.

Thanks to all the colleagues of the Applied Nuclear Physics division for the nice fika and lunch discussion.

A special thanks goes to Andrea, Henrik, Bill, Katerina, Nico, Maaike, Tuur: thank you for your beautiful friendship.

Grazie alla mia famiglia per sostenermi a distanza con tutto l'affetto possibile.

Gracias Cristina por todo el amor que ponés en mi vida.

References

- [1] J. Onega and G. Van Oost, *Energy for future centuries:prospects for fusion power as a future energy source*, Transactions of Fusion Science and Technology 53 (2008) 3.
- [2] D. H. Crandall, *The scientific status of fusion*, Nucl. Instrum. Methods Phys. Res. B 42 (1989) 409.
- [3] F. F. Chen, *Introduction to plasma physics and controlled fusion, Volume 1: Plasma physics*, 2nd edition, Plenum Press, New York, 1984.
- [4] J. Wesson, *Tokamaks*, 2nd edition, Clarendon Press, Oxford, 1997.
- [5] M. A. Pick and Jet Team, *The technological achievements and experience at JET*, Fusion Eng. Des. 46 (1999) 291.
- [6] B. Wolle, *Tokamak plasma diagnostics based on measured neutron signals*, Physics Reports 312 (1999) 1.
- [7] H. Brysk, *Fusion neutron energies and spectra*, Plasma Phys. 15 (1973) 611.
- [8] E. Andersson Sundén et al., *The thin-foil magnetic proton recoil neutron spectrometer MPRu at JET*, Nucl. Instrum. Methods Phys. Res. A 610 (2009) 682.
- [9] M. Gatū Johnson et al., *The 2.5-MeV neutron time-of-flight spectrometer TOFOR for experiments at JET*, Nucl. Instrum. Methods Phys. Res. A 591 (2008) 417.
- [10] G.F. Knoll, *Radiation detection and measurements*, John Wiley and Sons, Inc., New York 2000.
- [11] V. V. Verbinski et al., *Calibration of an organic scintillator for neutron spectrometry*, Nucl. Instr. and Meth. 65 (1968) 8.
- [12] <http://www.eljentechology.com/index.php/products/liquid-scintillators/71-ej-301> (Accessed 21 April 2015).
- [13] C. Cazzaniga et al., *Single crystal diamond detector measurements of deuterium-deuterium and deuterium-tritium neutrons in Joint European Torus fusion plasmas*, Rev. Sci. Instrum. 85 (2014) 043506.
- [14] <http://pdf.datasheetcatalog.com/datasheet/hamamatsu/R5611-01.pdf> (Accessed 21 April 2015).
- [15] <http://spdevices.com/index.php/adq214> (Accessed 21 April 2015).

- [16] See <http://mcnpx.lanl.gov/> for MCNPX code (Accessed 21 April 2015).
- [17] Code hosted on <https://github.com/FedericoBinda/dacsim> (Accessed 21 April 2015).
- [18] Documentation of the code hosted on <https://dacsim.readthedocs.org> (Accessed 21 April 2015).
- [19] S. O. Flyckt and C. Marmonier *Photomultiplier Tubes: Principles and Applications*, Photonis, Brive, France (2002).
- [20] M. Cecconello et al., *The 2.5 MeV neutron flux monitor for MAST*, Nucl. Instrum. Methods Phys. Res. A 753 (2014) 72.
- [21] J. P. H. E. Ongena et al., *Numerical transport codes*, Trans. Fusion Sci. Technol. 61 2T (2012) 180.
- [22] L. Ballabio. *Calculation and Measurement of the Neutron Emission Spectrum due to Thermonuclear and Higher-Order Reactions in Tokamak Plasmas*, PhD thesis, Uppsala University (2003).
- [23] C. Hellesen et al., *Fast-ion distributions from third harmonic ICRF heating studied with neutron emission spectroscopy* , Nucl. Fusion 53 (2013) 113009.
- [24] T. H. Stix, *Fast-wave heating of a two-component plasma*, Nucl. Fusion 15 (1975) 737.
- [25] N. P. Hawkes et al., *Measurements of the proton light output function of the organic liquid scintillator NE213 in several detectors*, Nucl. Instrum. Methods Phys. Res. A 476 (2002) 190.
- [26] G. Dietze and H. Klein, *NRESP4 and NEFF4: Monte Carlo Codes for the Calculation of Neutron Response Functions and Detection Efficiencies for NE213 Scintillation Detectors*, PTB Report PTB-ND-22, 1982, ISSN 0572-7170.